TUHH
Technische Universität Hamburg

Master Thesis

Development and Implementation of a Manufacturing Concept for a Low-Cost Inductive Conductivity Sensor for Maritime Applications

Author
Finn Jannek Klar

December 9, 2021

1st Examiner:	Prof. Dr.-Ing. Thorsten A. Kern
2nd Examiner:	Prof. Dr.-Ing. Heiko Falk
Supervisor:	M. Sc. Julius Harms

at

INSTITUTE
FOR MECHATRONICS
IN MECHANICS

Task Description

For marine and climate research, the measurement of ocean currents is essential. The density of water, i.e., the salinity and the temperature, strongly influence current velocities. The high-precision measuring instruments used in oceanography to determine density are often expensive and difficult to use. The Institute of Mechatronics is working on a simple, low-cost sensor buoy in the IoT standard, enabling a high quantity of measurements and thus providing measurement data with higher spatial resolution. One of the major hurdles is the reliable long-term determination of salinity by conductivity sensors.

Inductive conductivity sensors offer a significant advantage over contact-based measurement methods in the long-term stability of the measurement results. However, the production is more cost-intensive, and the energy consumption is higher compared to conductivity sensors. Within the scope of this master thesis, the existing research and sensor concepts of the Institute of Mechatronics are to be connected. Based on extensive preliminary investigations from various works, a production-ready inductive conductivity sensor with particular strengths in manufacturing costs, energy efficiency, and long-term use is to be developed.

At the beginning of the master thesis, the thematic familiarization and the understanding of the existing concepts and sensor models are carried out. Based on an existing sensor design, an optimized implementation should be developed, which includes the electrical design of the sensor coils, the measuring circuit's implementation, and a housing design for productions in larger quantities. The master thesis should result in a complete manufacturing concept for a low-cost inductive conductivity sensor, forming the basis for series production. In addition to excitation, sampling, and conversion, the integrated measuring circuit should also contain a microcontroller for which suitable calibration and evaluation software is programmed.

Statutory Declaration

I declare that I have prepared my Master Thesis with the title

Development and Implementation of a Manufacturing Concept for a Low-Cost Inductive Conductivity Sensor for Maritime Applications

submitted to Prof. Dr.-Ing. Thorsten A. Kern independently and without the use of other than the indicated aids and that I have marked all passages that I have taken verbatim or in spirit from publications as such. The thesis has not yet been submitted to any examination authority in the same or similar form or in excerpts. I assure that the submitted written version corresponds to the version stored on the enclosed medium.

_____

Date and signature

Contents

List Of Symbols **iii**

1 Introduction **1**

2 Fundamentals and State of the Art **2**
2.1 Conductivity and Salinity 2
2.2 Practical Salinity Scale 1978 (PSS-78) 3
2.3 Transformer Type Inductive Conductivity Sensor - TICS 4

3 Concept and Solution Design **9**
3.1 Requirements 9
3.2 Functional Decomposition 10
3.3 Concepts 10
3.3.1 Signal Generation 11
3.3.2 Transformer Type Inductive Conductivity Sensor 14
3.3.3 Signal Acquisition 20
3.3.4 Data Processing 22
3.3.5 Handling and Communications 23
3.4 Final Concept 24

4 Implementation **26**
4.1 Physical Sensor Hardware 26
4.1.1 Voltage Reference for ADC and DAC 26
4.1.2 Dimensioning TICS 27
4.1.3 Gate Driver and Measurement Circuit for TICS 27
4.1.4 DC-DC Converter 31
4.1.5 Sensor Schema 31
4.1.6 PCB Design 32
4.2 Software Design - Principle of Operation 33
4.2.1 Calibration Algorithm 34
4.2.2 State Machine Sensor Module 35
4.2.3 UART Transfers 35
4.2.4 DAC 36
4.2.5 ADC 36
4.3 System Validation 36
4.3.1 Test of Shielding 36

5 Results and Analysis **40**
5.1 Test of Known Resistors 40
5.2 Determination of the cell constant 41

6 Conclusion and Outlook **49**

A Appendix **51**
A.1 Schematic 51
A.2 Bill of Materials 54
A.3 Layout 55
A.4 Determination of Desired Sensor Resolution 57
A.5 Equation for TICS Sensor Current 58
A.6 Influence of k on frequency response 61
A.7 Effect of Mutual Coupling in Range of MHz 63
A.8 Simplifications on k-Factor impact 64

List Of Symbols

Symbol	Quantity	Unit
A	Area	m^2
C	Capacity	F
$k_{\mathbf{cell}}$	Cell constant	
$k_{\mathbf{sensor}}$	Sensor constant	
K_{15}	Conductivity ratio at 15 °C and 1 ATM	
κ	Conductivity	$mS\,cm^{-1}$
R_r	Conductivity ratio	
I	Current	A
R	Electrical resistance	Ω
L	Inductance	H
M	Mutual inductance	H
l	length	m
P	Power	W
p	Pressure	dbar
T	Temperature	°C
N	Turn number of coil	
f	Frequency	Hz
R_m	Magnetic resistance	$A V^{-1} s^{-1}$
k	Mutual coupling factor	
S	Practical salinity	
ω	Angular velocity	$rad\,s^{-1}$
U	Voltage	V

1 Introduction

The consequences of progressive climate change are becoming increasingly apparent. Heavy rainfall events [33] and cold snaps [12] due to a changing jet stream are the most recent consequences.

A study [6] from August 2021 shows a gradual weakening of the Atlantic Meridional Overturning Circulation toward a critical transition. Its influence play an essential role in the Earth's climate [7] through ocean meridional heat transport. This meridional overturning circulation is prone to changes in salinity [13].

Measuring in situ conductivity of seawater is crucial to determine the local value of seawater salinity, prone to freshwater fluxes, changes in sea ice, and others affect [13, p. 159].

So far, only satellites allow high spatial resolution. However, since satellite data are less accurate compared to in situ data, the demand for acquisition with a high spatial resolution is given. Therefore, developing low-cost conductivity sensors to determine salinity in the surface water is of interest.

This thesis begins with a brief introduction to conductivity, salinity, and possible sensor setups for conductivity measurements in marine waters with Section 2.

The second part covers a concept and solution design. Within this framework, functional decomposition of conductivity measurement is conducted. Challenges are analyzed, and solutions are developed based on the sub-functions in Section 3.

The Hardware is then implemented based on the previously developed concept in Section 4. The implementation includes the design of physical components, a circuit design, and a PCB design.

The fourth part covers the software. The verification of designed hardware requires test functions discussed in this section. The operation, calibration, and measurement description conclude this chapter.

A summary and an outlook conclude the thesis in Section 6.

2 Fundamentals and State of the Art

This chapter starts with a brief introduction to the measurands conductivity and salinity (Section 2.1). Converting conductivity data is done by using the 'Practical Salinity Scale 1978' and the temperature value of the sampled water (Section 2.2). A section about conductivity sensor models concludes this chapter.

2.1 Conductivity and Salinity

The current density $\vec{J}$ is proportional to the product of conductivity κ and field strength $\vec{E}$ of the current-carrying medium [2, p. 89]. It depends on the number n, the mobility μ_e, and the charge e of the carriers present according to

$$\kappa = ne\mu_e. \tag{1}$$

Changes in mobility by temperature or quantity of charges carriers like adding ions to solutions change the conductivity. The conductivity thus provides information about the resistance of the electrical conductor with known dimensions ([2, p. 92]),

$$R = \frac{l}{\kappa A} \tag{2}$$

applies.

The term salinity S (also referred to as S_P) used in this document refers to the 'Practical Salinity 1978' for seawater by the Joint Panel on Oceanographic Tables and Standards (JPOTS), which is also known as Practical Salinity.
Salinity S is defined on the electrical conductivity ratio K_{15} of sampled seawater to that of potassium chloride (KCl) solution. This solution contains 32.4356 gKCl in 1 kg of the solution. K_{15} requires sampling of seawater and KCl solution at 15 °C and the pressure of one standard atmosphere. By definition, a value of K_{15}=1 corresponds to S=35. [20] [32, p. 43]
UNESCO states in the report *the International system of units (SI) in oceanography* ([32, p. 44]) Practical Salinity is a ratio of two electrical conductivity. Thus its unit has no dimension.
The International Thermodynamic Equation Of Seawater - 2010 (TEOS-10) is the latest approach to the calculation of thermodynamic properties of seawater. This approach uses newer definitions of salinity. Continuing in using Practical Salinity ensures continuity in national and international databases. [11, p. 4, 10]

2.2 Practical Salinity Scale 1978 (PSS-78)

The International system of units (SI) in oceanography ([32, p. 43]) states the equation to calculate Practical Salinity based on the previously introduced conductivity ratio K_{15} to be

$$S = a_0 + a_1 K_{15}^{1/2} + a_2 K_{15} + a_3 K_{15}^{3/2} + a_4 K_{15}^2 + a_5 K_{15}^{5/2} \tag{3}$$

Table 2 lists the coefficients a_i.

Table 2: *Coefficients for PSS-78 formulae*

i	a_i	b_i	c_i	d_i	e_i
0	0.0080	0.0005	$6.766097x10^{-1}$		
1	−0.1692	−0.0056	$2.00564x10^{-2}$	$3.426x10^{-2}$	$2.070x10^{-5}$
2	25.3851	−0.0066	$1.104259x10^{-4}$	$4.464x10^{-4}$	$-6.370x10^{-10}$
3	14.0941	−0.0375	$-6.9698x10^{-7}$	$4.215x10^{-1}$	$3.989x10^{-15}$
4	−7.0261	0.0636	$1.0031x10^{-9}$	$-3.107x10^{-3}$	
5	2.7081	−0.0144			

Lewis ([20]) and UNESCO ([11, p. 147]) provide the formulae for in-situ measurement. In contrast to the definition of S based on the ratio K_{15}

$$K_{15} = \frac{\kappa(S,15\,°C,0)}{\kappa(35,15\,°C,0)}, \tag{4}$$

field measurements result in the conductivity ratio R_r

$$\begin{aligned} R_r = \frac{\kappa(S,T,p)}{\kappa(35,15\,°C,0)} &= \frac{\kappa(S,T,p)}{\kappa(S,T,0)} \cdot \frac{\kappa(S,T,0)}{\kappa(35,T,0)} \cdot \frac{\kappa(35,T,0)}{\kappa(35,15\,°C,0)} \\ &= R_{rp} \cdot R_{rT} \cdot r_{rT} \end{aligned} \tag{5}$$

due to variations in temperature T and pressure p to those in a controlled environment. The polynomial

$$r_{rT} = \sum_{i=0}^{4} c_i (T)^i \tag{6}$$

describes the factor r_{rT}. R_{rp} is a function of p, R_r, and T combined to

$$R_{rp} = 1 + \frac{\sum_{i=1}^{3} e_i p^i}{1 + d_1 T + d_2 T^2 + R_r(d_3 + d_4 T)}. \tag{7}$$

With R_{rT} being

$$R_{rT} = \frac{R_r}{R_{rp} r_T}, \tag{8}$$

the following function of R_{rt} and T with $k = 0.0162$ determines S to

$$S = \sum_{i=0}^{5} a_i (R_{rT})^{i/2} + \frac{T-15}{1+k(T-15)} \sum_{i=0}^{5} b_i (R_{rT})^{i/2}. \tag{9}$$

These formulae are valid within the range -2 °C≤ T ≤35 °C, 0 ≤ p ≤ 10000 dbar, and $2 < S < 42$. The TEOS-10 website ([28]) holds functions (in MATLAB/C/Others) for calculations in the context of PSS-78. The documentation lists the reference conductivity κ(35,15,0) to be

$$\kappa(35,15,0) = 42.9140\ mS/cm. \tag{10}$$

2.3 Transformer Type Inductive Conductivity Sensor - TICS

A TICS consists of one or two toroidal coils isolated in water by a housing. Coil 1 induces a current into the water; coil two measures this current.

Electromagnetic induction (Figure 1) is the physical effect transformer type inductive conductivity sensors used to determine the medium conductivity. An AC current $i_1(t)$ in a conductor loop creates a magnetic flux $\phi_{11}(t)$. A part of this magnetic flux (ϕ_{21}) passes through a second conductor loop. In the second loop, a voltage $u_{2ind}(t)$ is induced depending on the time change of the flux passing through it.

$$u_{2ind} = -\frac{d\phi_{21}}{dt} = -L_{21}\frac{di_1}{dt}. \tag{11}$$

The induced voltage causes a current flow in the second conductor loop. This also generates a magnetic flux, namely ϕ_{22}. The part which flows through the first coil is ϕ_{12}. The described case is formally described in an extended form by

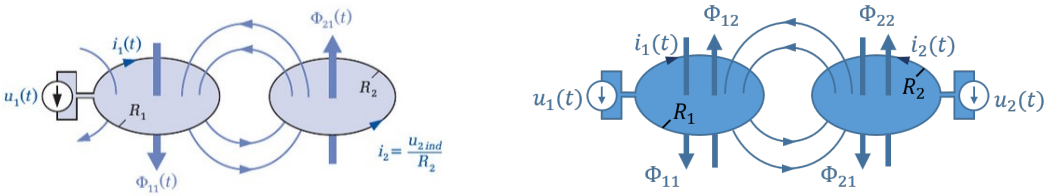

(a) **(b)**

Figure 1: *Electromagnetic induction: Coupled circuits by [2, p. 251]* ***(a)****; Coupled circuits with opposing flows according to [2, p. 253]* ***(b)****.*

$$\begin{aligned} u_1 &= R_1 i_1 + \frac{d}{dt}\left(\phi_{11} - \phi 12\right) = R_1 i_1 + L_{11}\frac{di_1}{dt} - L_{12}\frac{di_2}{dt} \\ u_1 &= R_2 i_2 + \frac{d}{dt}\left(\phi_{22} - \phi 21\right) = R_2 i_1 + L_{22}\frac{di_2}{dt} - L_{21}\frac{di_i}{dt}. \end{aligned} \tag{12}$$

A more detailed description of induction can be found in [2, pp. 250-254]. In the marine application, the water acts as the second circuit, and ferrite cores are used to generate an increased[1] magnetic flux. Since the path of the ionic current $i_2 = i_w$ is not known in the water, Equation (2) is simplified. A cell constant k_{cell} replaces the unknown dimensions linking resistance R_w and conductivity according to

$$R_w = \frac{l_w}{\kappa A_w} = \frac{k_{\text{cell}}}{\kappa}. \tag{13}$$

Applications with three involved conductor loops exist (Figure 2). This is interesting for applications where the exciting signal is many times larger than the influence of the mutual inductance.

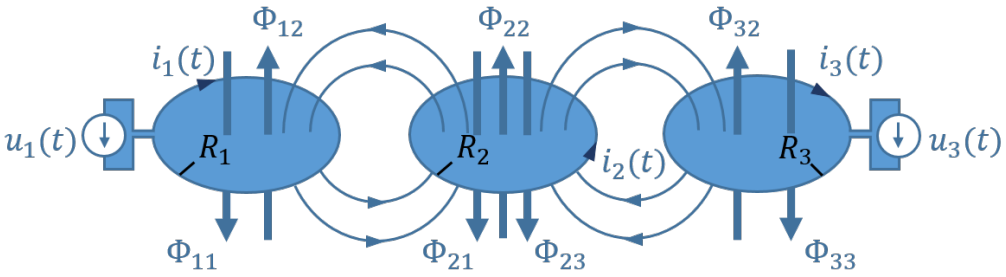

Figure 2: *Electromagnetic induction on three circuits*

Striggow *et al.*. discussed in [14, 15] different setups for conductivity sensors used in oceanographic work. Among the group of sensors feasible for the task, capacitive sensors and sensors requiring exposed electrodes are affected by polarization and

[1] Compared to a magnetic flux without ferrite cores

fouling, reducing long-term stability. Inductive sensors used for in-situ measurements do not require physical contact with the electrolytic solution. The permeability of the required transformer core(s) is variable to temperature and pressure. Striggow *et al.*. performed a theoretical analysis of three different inductive sensor models.
A single transformer consists of a toroid core with one coil made of wire, the surrounding liquid forming the second coil. Sensor output current I_1 derived in [14] is

$$I_1 = \left(\frac{1}{N_1^2 R_w} + \frac{1}{j\omega L_1} \right) U_1, \tag{14}$$

where N_1 is the number of turns of the primary coil, R_w the water resistance, L_1 the self-inductance of the primary coil, and U_1 the primary voltage. The real part of sensor output is free of influence from changes in permeability.

Striggow *et al.*. [14] suggested six different approaches to achieve a reading of the water conductivity. These require either multiple measurements simultaneously, the precise matching of electrical components, or a rectangular input voltage combined with timed measurements on the sensor signal.

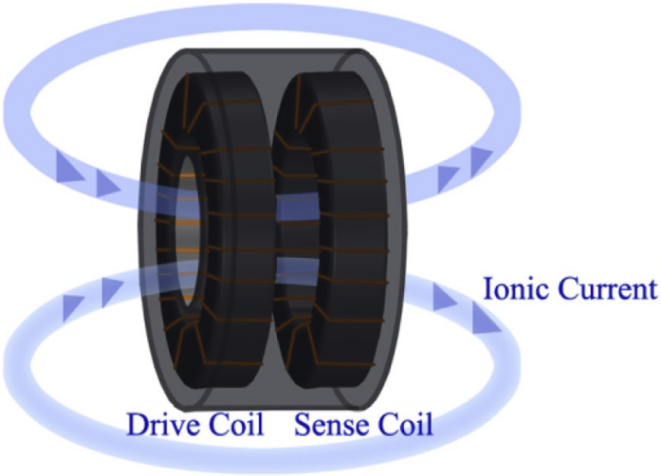

Figure 3: *The double transformer for conductivity measurement [14]*

Two transformers linked through a water loop (Figure 3) form a double transformer. The water acts as a secondary coil at the first transformer and as a primary coil at the second. If the only coupling of these transformers is by the water loop (Figure 4), the sensor output signal U_4 is linked to R_W by

$$U_4 = \frac{N_4}{N_1} \frac{1}{1 + N_4^2 R_W \left(\frac{1}{R_R} + \frac{1}{j\omega L_4} \right)} U_1. \tag{15}$$

Indices of number four correspond to the secondary coil of the second transformer. By shunting terminating resistor R_R a short-circuit current $I_{4,S}$ independent of inductance L_{44} is achieved:

$$I_{4,S} = \lim_{R_R \to 0} (U_4/R_R) = \frac{1}{N_1 N_4 R_W} U_1. \tag{16}$$

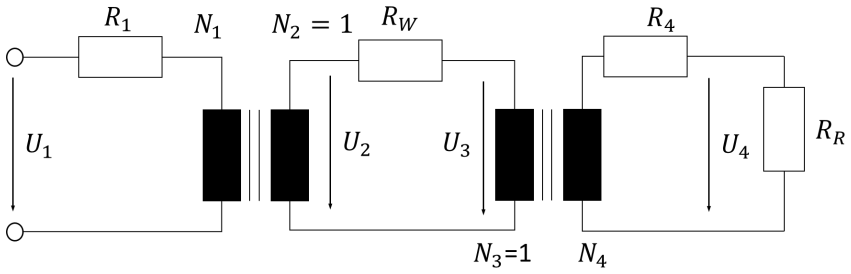

Figure 4: *Circuit of the double transformer for conductivity measurement according to [14]*

Striggow *et al.*. ([14, 15]) analyzed a third setup based on the double transformer with an additional loop, such that water loop and additional loop work in push-pull operation (Figure 5).

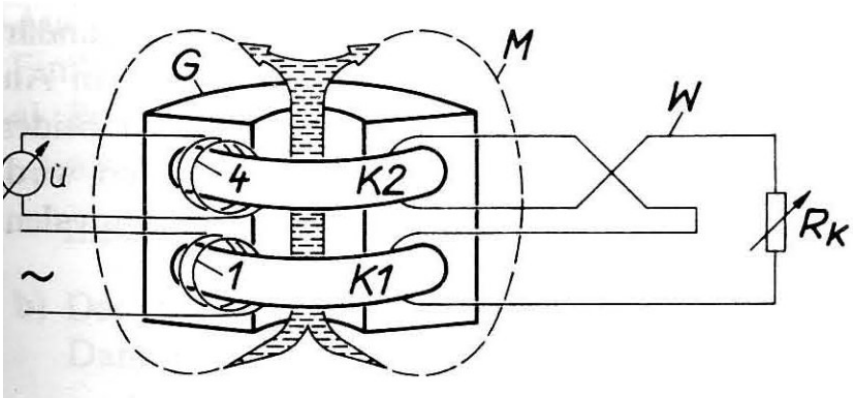

Figure 5: *The double transformer with an additional loop according by [14]*

The sensor output signal based on the circuit (Figure 6) with an additional loop resistor R_C is

$$U_4 = \frac{N_4}{N_1} \frac{1}{1 + N_4^2 \frac{R_W \cdot R_C}{R_W + R_C} \left(\frac{1}{R_R} + \frac{1}{j\omega L_4} \right)} \frac{R_C - R_W}{R_C + R_W} U_1. \tag{17}$$

Depending on the design of the loop resistor, different behaviors of the sensor come to use. In terms of short-circuit current

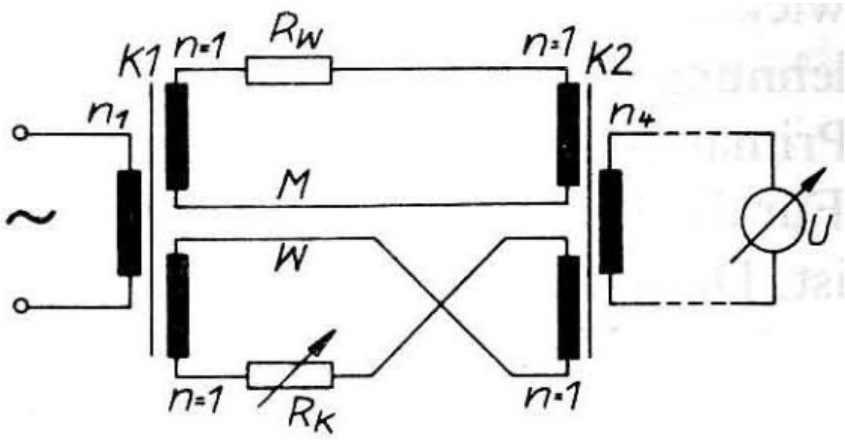

Figure 6: *Circuit of the double transformer with additional loop according by [14]*

$$I_{4,S} = \lim_{R_R \to 0} (U_4 / R_R) = \frac{1}{N_1 N_4} \left(\frac{1}{R_W} - \frac{1}{R_C} \right) U_1. \tag{18}$$

A change of R_W can be interpreted as a shift of the conductivity zero point. Other approaches use a tuned capacitance to decouple the phase shift of primary and secondary voltage (open-circuit operation, $R_R = \infty$) or secondary current from the primary voltage (short-circuit operation, $R_R = 0$) from the inductance.

The presented approaches use simplifications such as neglecting coil resistance and direct coupling of the two coils. In the course of this thesis, a sensor based on the double transformer model will be developed. Section 3.3.2 discusses the impact of those simplifications and the effects of differential shielding and wire resistance.

3 Concept and Solution Design

Programs such as the European Union's *Copernicus* satellite-based Earth observation program or the U.S. National Oceanic Atmospheric Administration's Global Drifter Program (GDP) monitor the world's oceans. Satellites require calibration of their sensors, provided by observation areas with sufficient data density. Drifters registered with the GDP are deployed in various places around the globe providing single point data ([10]). Measuring salinity in a dense mesh using self sufficient sensor buoys requires low-cost and low-power conductivity sensors. Therefore the target of this thesis work is the development of a production ready embedded TICS designed for oceanographic use. The development of a solution is based on the requirements presented in Section 3.1. A functional decomposition is performed (Section 3.2). The chapter concludes with the final concept in Section 3.4.

3.1 Requirements

A production-ready inductive conductivity sensor of low costs and low power consumption will be developed for long-term use in surface waters on a low-cost sensor buoy. Converting conductivity measurements to Practical Salinity using the formulas presented in Section 2.2 requires temperature readings. An additional temperature sensor provides these readings. Therefore, it is anticipated that the conversion of temperature data and conductivity values will be performed externally (on the buoy).

The sea surface temperature of the oceans ranges between -2 °C and 35 °C [24]. The required conductivity measurement range is determined to be 2 mS/cm to 75 mS/cm (Table 3[2]).

Table 3: *Range of conductivity calculated by TEOS-10 function with listed inputs*

S	T [°C]	p [dbar]	κ [mS/cm]
2	−2	10.1325	1.9
42	35	10.1325	74.9

The desired accuracy is 0.05 on the PSS-78, which corresponds to a minimum of 0.0345 mS/cm (Section A.4). Table 4 summarizes the requirements for the sensor.

[2] 'gsw_C_from_SP.m', [28]

Table 4: *Table of requirements*

Name	Value
Conductivity range	2 mS/cm - 75 mS/cm
Accuracy	0.0345 mS/cm | < 0.05 on PSS-78
Low cost	yes
Low power	yes
Small size	yes
Long-term operation	>1 Year

3.2 Functional Decomposition

The overall conductivity measurement function consists of several sub-functions. The active measurement requires an alternating current to generate a magnetic flux that interacts with the water. The alternating current requires the signal generation sub-function. The alternating current then generates a magnetic flux that generates an ionic flux in the water, which generates a magnetic flux that generates a third current, the measurement signal. TICS represents implementing the described signal transformation, which is the second sub-function. This so-generated signal needs to be acquired for further processing and evaluation — the task of signal acquisition in the third sub-function. The acquired signal data is processed on a microcontroller and converted into a conductance, covered in the sub-function of data processing. Finally, the determined conductance must be temporarily stored, or the data stream must be output and processed. Thus handling and communications is the last sub-function.

An overview of these sub-functions is shown in Figure 7.

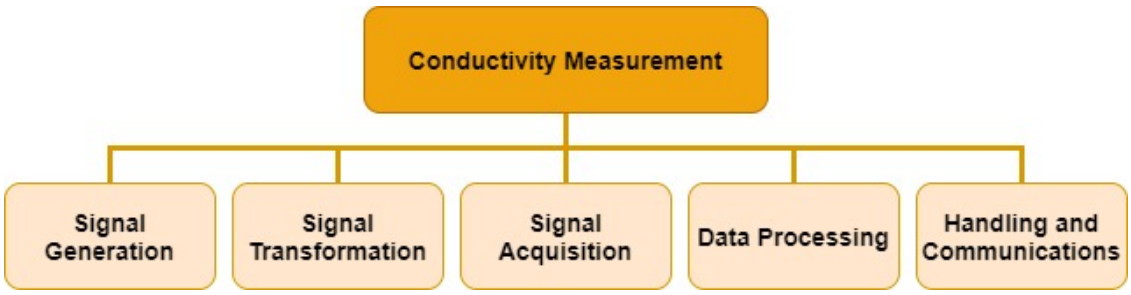

Figure 7: *Functional decomposition of conductivity sensor*

3.3 Concepts

The following sections govern the previously identified sub-functions in more detail. A closer look reveals requirements and possible solutions. The conclusions at the end of

the investigations for each sub-function summarize the results.

3.3.1 Signal Generation

Section 2.3 shows different approaches to eliminate the influence of changing core permeability on the sensor signal on different setups of TICS due to pressure and temperature effects. The expected spectrum of the noise is not known. Evaluating the measurement signal in the frequency domain allows an almost noise-free analysis. This evaluation requires a sensor signal of known frequency. Striggow and Dankert propose an approach on using a rectangular input voltage to bypass the influence of core permeability on the output signal [14, p. 31]. The sensor integrates this voltage into a ramped sensor output current, forming a sawtooth signal that jumps according to the input voltage. Changes in permeability do not influence the constant section of the rectangular signal. The peaks of this function correspond to the conductivity of the solution. Evaluating the peaks in the signal in the time domain is prone to noise.

Another option is to use a sweep. An extended view of the transmission channel TICS in the frequency domain shows that the phase has an intolerable error due to temperature-induced permeability changes. For this reason, and because a noise-corrected peak-to-peak evaluation of the signal is sufficient (see Equation (16)), a sweep is omitted. Bode plots and figures showing the phase error can be found in the appendix in Section A.6 Figure 47.

The signal required for excitation of TICS other than the single transformer version requires a sinusoidal wave. Previous publications on TICS ([16, 17, 25]) uses excitation signals of frequencies ≤30 kHz. A sine wave signal can be generated using various methods.

Analog Oscillator
An analog circuit can generate an oscillating signal. Therefore a feedback system of loop gain ≥ 1 and phase rotation of zero or multiple of 2π is required [19, p. 459]. Reducing the loop gain of the circuit to one at the desired frequency by additional circuitry shown in [19, p. 460] locks the oscillation amplitude. This approach requires a hardware design of oscillating circuit and amplitude regulating circuit. Figure 8 displays a setup for a Wien-bridge oscillator.

Square Wave
Another option to generate a sine wave is filtering a square wave of the desired frequency, according to the Fourier-Series ([19, p. 285])

$$f(t) = \frac{a_0}{2} + \sum_{n=1}^{\infty} \left(a_n cos(n\omega t) + b_n sin(n\omega t) \right), \tag{19}$$

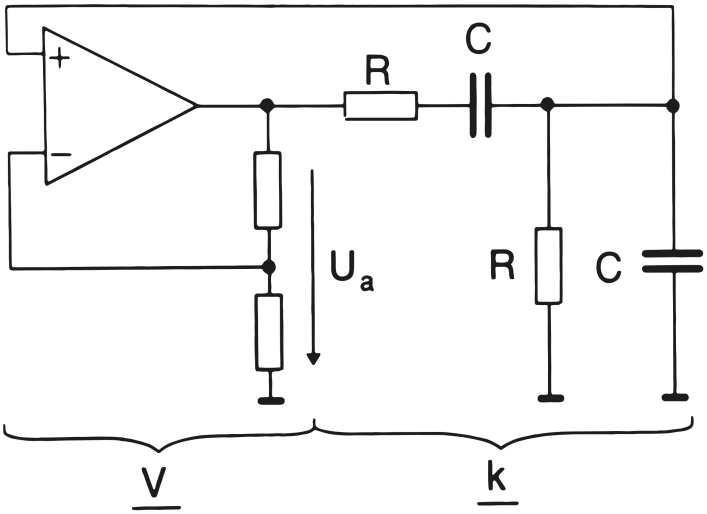

Figure 8: *Wien-bridge oscillator*

using

$$a_0 = \frac{1}{\pi}\int_{-\pi}^{\pi} f(t)\,\mathrm{d}t, a_n = \frac{1}{\pi}\int_{-\pi}^{\pi} f(t)cos(n\omega t)\,\mathrm{d}t, b_n = \frac{1}{\pi}\int_{-\pi}^{\pi} f(t)sin(n\omega t)\,\mathrm{d}t \tag{20}$$

to decomposed the square wave of amplitude h to

$$f(t) = \frac{4h}{\pi}\sum_{n=1}^{\infty}\frac{sin((2n-1)\omega t)}{2n-1}. \tag{21}$$

Thus, a low-pass filter with a cut-off frequency a little above the desired frequency can be used to attenuate multiples of the base frequency. Such a low-pass filter of higher order is implemented by lining up RC-low-pass filters. A timer altering an output port of an MCU generates the desired square wave.

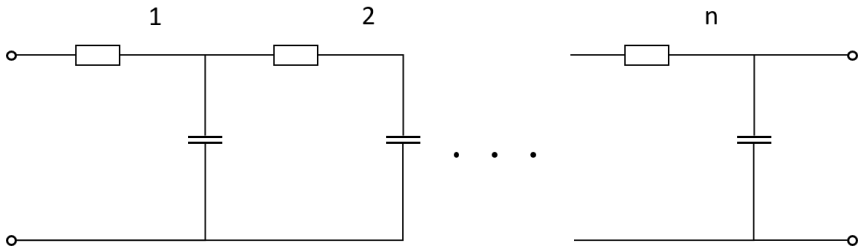

Figure 9: *Low-pass filter of order n*

PWM Signal

Tsai ([31]) shows the generation of a sine wave using a low-pass filter on a modulated

PWM signal. An MCU continuously generates a time-varying PWM. The pulse width is determined according to n sample points of a sine wave and a low-pass filter is used to get a sine wave. According to the application report, the frequency of the desired signal f_O depends on the number of samples n and the PWM frequency F_{PWM}

$$f_O = \frac{F_{PWM}}{n}. \tag{22}$$

Arbitrary Waveform Generator - AWG

Composing a function from individual data points is the work of an arbitrary waveform generator [29, p. 896]. A MCU calculates the desired signal as a set of n data points and stores it into it's RAM. By periodical incrementing RAM's address the DAC approximates the original function. The output signal is smoothed by a low-pass filter to retrieve a sine function if necessary. The counter incrementing clock frequency determines the frequency of the output signal.

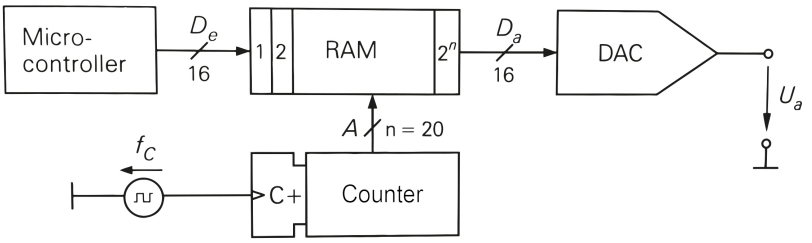

Figure 10: *Architecture AWG according to [29, p. 897]*

Direct Digital Synthesis - DDS

[29, p. 897] describes the method of Direct Digital Synthesis. The ROM of a DDS chip stores a quarter of a sine function, the ROM's address represents the phase angle of that function. A phase accumulator generates the address, increasing the phase by a defined phase increment. The data point stored in the address is converted using DAC. To change the frequency of the output signal, the phase increment is changed. In applications requiring frequency modulation or phase modulation, DDS requires less effort compared to AWG.

Conclusion

The methods presented are compared below in three categories. These are the requirements for the circuit design and the resource requirements of an MCU. Finally, the possibility to change the frequency in retrospect to hardware implementation is of interest.

Among the five signal generation methods presented, the first three require an electrical circuit tailored to generate the desired signal. The analog oscillator demands the most on circuit design because of the need to limit amplitude at the desired frequency. In the

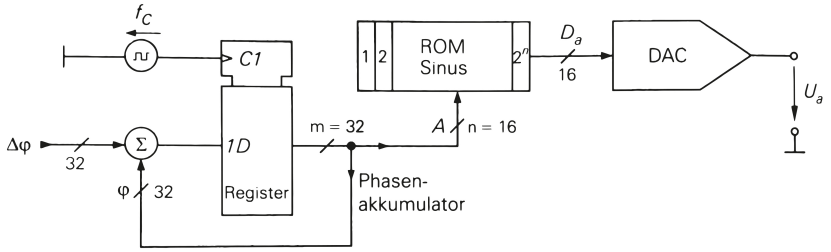

Figure 11: *Architecture DDS according to [29, p. 898]*

case of DAC-based signal generation (AWG and DDS), a low pass filter for smoothing is mandatory. The analog oscillator does not require any resources of the MCU. Among the remaining solutions, the generation of a square wave signal requires the least resources. Assuming that the generation of a PWM only requires the input of the pulse width and the DAC only receives the digital value, PWM, AWG and DDS requires a similar amount of resources. With assembled hardware, solely AWG, and DDS allow the signal frequency to be changed. Considering AWG and DDS being the most feasible choices for signal generation (Table 5), AWG is chosen as the architecture of DDS is more complex to implement (compare Figure 10 and Figure 11).

Table 5: *Performance of solutions on signal generation*

Category	Analog oscillator	Square wave	PWM	AWG	DDS
Circuit design		+	+	++	++
MCU resources	++	+			
Variable frequency				++	++
$\sum$	++	++	+	++++	++++

3.3.2 Transformer Type Inductive Conductivity Sensor

The sensor output current of the double transformer is free of the effect of permeability and proportional to water conductivity (Equation (16)). A shift of conductivity zero-point introduced by an additional loop (Equation (18)) requires matching of loop resistance and increasing the sensor complexity. Thus the use of a double transformer similar to those in previous works ([8, 16, 17, 34]) is continued.

Simulation Data

This subchapter contains simulations of ETICS models. The model used for the simulation is based on the setups in [16, 17]. Table 6 lists the parameters used. The cell constant depends on the flow of ionic current in the water. Since this expression is unknown, the simulations in this section use a cell constant of unity.

Table 6: *Parameters for simulations on TICS*

Parameter name	Value
Core permeability	10,000
Winding primary coil	10
Winding secondary coil	10
Excitation frequency	10 kHz
Drive voltage amplitude	1 V
Conductivity of water	75 mS/cm
Radius of copper wire	0.3 mm
Core inner diameter	13.5 mm
Core outer diameter	26.6 mm
Core height	11 mm
Distance coils	1 mm
Cell constant	1

Simplifications on TICS

Theoretical analyses done by Striggow et. al [14] (Section 2.3) used in [17] neglect the resistance of the coils. A comparison of the systems described by current $I_{4,S}$ in Equation (16) and a less simplified equation for $I_{4,S}$ (see Section A.5) is performed in MATLAB.

Figure 12 displays the bode plot for the simplified system and non simplified systems with coil cores of different permeability. The effect of coil resistance is with a maximum impact of -0.01 dB considerable low. The analysis of a system exposed to temperature changes similar to those of a field application show that the effect of the coil wire cannot be neglected (Figure 13). An maximum absolute error of 0.04 % corresponds to a deviation of 30 µS/cm, which is below the required accuracy in Table 4. A temperature compensation in software can reduce the offset.

Mutual Coupling of Primary and Secondary Coil on TICS

Striggow and Danker demand suppression of mutual coupling between the two sensor coils in [14]. A FEM simulation based on a TICS model gives information on the mutual inductance magnitude. Table 7 displays the results of the FEM simulation. The simulation data suggest that a plate has the most significant effect on shielding the coils and reduces the mutual inductance by a factor of five. Figure 15 shows the effect of mutual coupling between the two coils on the sensor current $I_{4,S}$. This plot empathizes the neglection of mutual coupling for an attenuating signal in the desired range of frequencies. The effect of M_{14} can not be neglected if the input voltage would oscillate in the range of MHz. Figure 48 in Section A.7 displays the influence at 10 MHz.

Effect of Core Windings on Performance

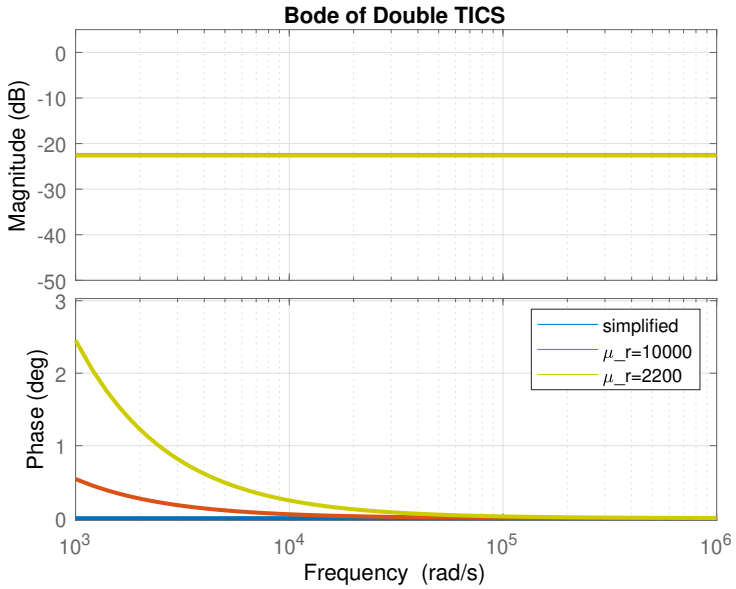

Figure 12: *Effect of simplification with respect to permeability*

Table 7: *Inductance and mutual inductance by the FEM simulation*

Parameter name	Value	ppm of Inductance	% of M_{14} (no shield)
Inductance	105.58 µH	100 %	
Mutual inductance (no shield)	3.84 nH	36.37 ppm	100 %
Mutual inductance (plate)	744.79 pH	7.05 ppm	19.40 %
Mutual inductance (outer cup)	1.06 nH	10.04 ppm	27.60 %
Mutual inductance (cup)	1.08 nH	10.23 ppm	28.13 %

The amplitude of the sensor signal (Equation (16)) is reciprocally influenced by the winding numbers of the coils. The equations Equation (23) and Equation (24) given in [17] can be used to describe the power consumption of the double transformer sensor (Figure 4). The assumptions $R_R = 0$, $R_1 << jL_1\omega$, $R_4 << jL_4\omega$, $N_2 = N_3 = 1$, and $k_{12} = k_{34} = 1$ are applied and the inductance are transformed according to Equation (52) and Equation (53) (see Section A.5). The result is Equation (25). Therefore reducing N_1 has the greatest effect on lowering the power consumption of TICS.

$$I_1 = \frac{A}{A\left(R_1 + jL_1\omega\right) + M_{12}^2\omega^2} U_1 \tag{23}$$

$$A = \frac{M_{34}^2\omega^2}{R_R + R_4 + jL_4\omega} + \left(R_W + jL_2\omega + jL_3\omega\right) \tag{24}$$

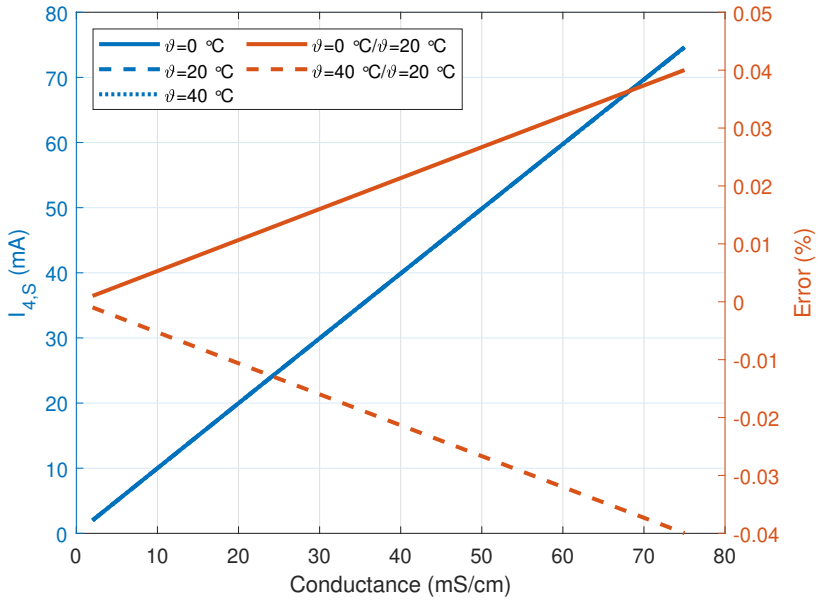

Figure 13: *Relative error on the sensor output current due to changes in temperature*

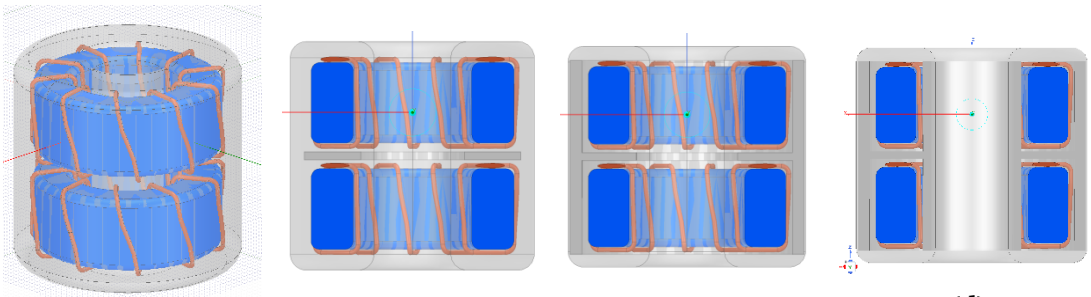

(a) **(b)** **(c)** **(d)**

Figure 14: *TICS with different shieldings: No shielding **(a)**; Plate **(b)**; Outer cup **(c)**; Cup **(d)**.*

$$I_1 = \frac{\omega - jR_W R_m}{N_1^2 R_W \omega} U_1 \tag{25}$$

Effect of k-Faktor on Sensor Output

Kang Hui *et al.* [17] derives the equations proposed in [14] by Striggow and Dankert with respect to the coupling between the water circuit and the coils. Kang Hui *et al.*. assume a coupling factor of $k = 1$. The Equation (23), Equation (24) and Equation (26) (from [17]) describe the relation of the ionic current in the water I_2 and the drive current U_1. Equation (27) represented the relationship between I_2 and I_4. The effect of the k-factor is derived using

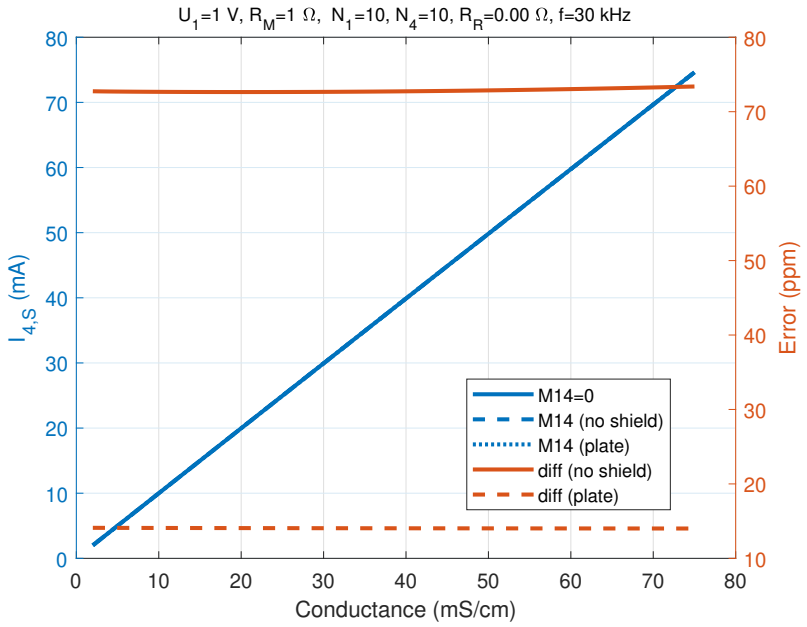

Figure 15: *Effect of M14*

$$I_2 = -\frac{jM_{12}\omega}{A} I_1, \tag{26}$$

$$I_4 = -\frac{jM_{34}\omega}{R_R + R_4 + jL_4\omega} I_2, \tag{27}$$

and previously used Equation (23) and Equation (24). MATLAB's symbolic toolbox is used to simplify the term obtained by merging the listed equations (Section A.8). The result is

$$I_4 = \frac{jR_m k_{12} k_{34}}{N_1 N_4 (k_{12}^2\omega + k_{34}^2\omega - 2\omega + jR_W R_m)} U_1. \tag{28}$$

This relationship shows a quadratic influence of the coupling factor, which increases at higher frequency. For the k-factors equal to one, the sensor current in Equation (16) is obtained. Since the effect of the k-factors does not scale with the water conductivity, a compensation is not required. The effect on drive current (Equation (23) contains M_{12} and M_{34}) and sensor current is relevant for sensor design. Figure 16 indicates that calculating circuit design parameters related to the current to and from the sensor requires the consideration of two different k-factors. Additional plots on the influence of the k-factors are given in Section A.6, where the optimal frequency f for attenuation is found to be 10 kHz.

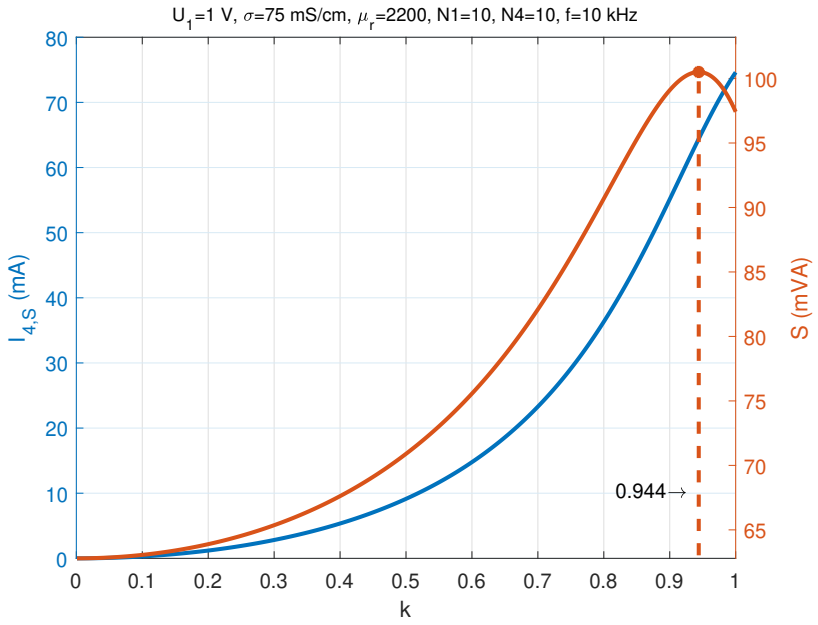

Figure 16: *Effect of k on power consumption and sensor signal*

Suitable Core Sizes

TDK offers a variety of torrid-shaped magnets feasible for TICS. Measuring conductivity does not require a permeability of $\mu_r = 10.000$ (Figure 12). The core material N87 ($\mu_r = 2.200$) is chosen due to its high availability and low cost at the coil supplier's site. An analysis of the core sizes offered ([22], parameters of uncoated cores) shows that the core parameter combination *25.3x14.8* is a good tradeoff of required power and core size. The core has the third-lowest power demand in comparison (Figure 17) and a core diameter smaller than 3 cm. Kandur [16] used cores of the same dimensions (Kandur lists dimensions of coated cores). The coils have a length of 10 mm.

Conclusion

Previous approaches do not consider the impact of coil resistance concerning temperature changes. A simulation on TICS shows these effects to be of nonlinear behavior to changes of temperature. These nonlinearities require a temperature-dependent offset compensation implemented in software. The effects of mutual coupling of the coils are insignificant for the desired application in the kHz frequency range. The transformer core with dimensions *25.3x14.8* is best suited for this application. When designing the electrical circuit, varying loads for different k-factors must be considered.

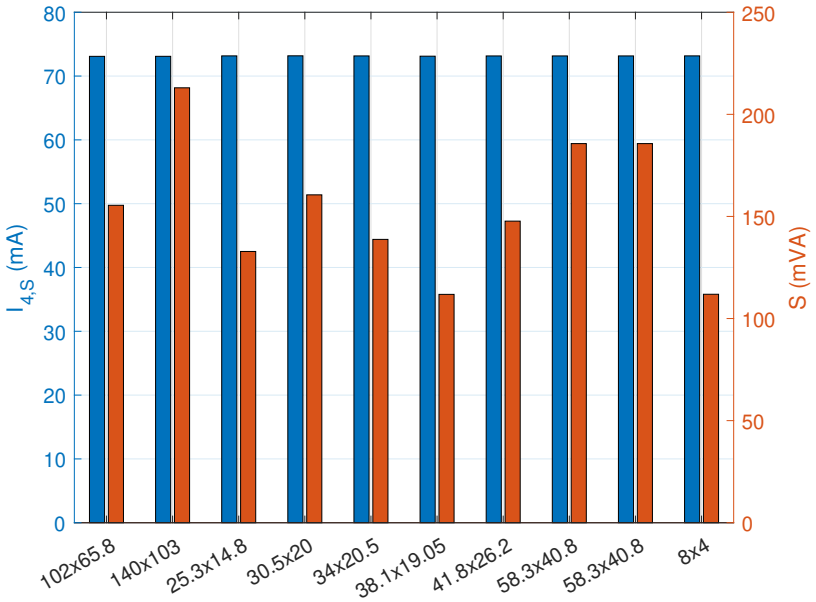

Figure 17: *Effect of core sizes on sensor signal and required power*

3.3.3 Signal Acquisition

The purpose of data acquisition is to convert the analog measurement signal (the current $I_{4,S}$) into a digital measurement value. The described sensor signal (Equation (15)) changes in reciprocal to conductivity. This behavior suffices a measurement of the sigla value. Transformation of analog signals to digital signals requires ADC. The input of ADCs is a voltage [29, p. 1032]. The signal acquisition sub-function consists of a current-voltage conversion and the subsequent conversion into a digital signal using an ADC.

Current-Voltage Conversion
The most straightforward approach to conversion is to use a resistor. The voltage across the resistor is measured. Since the sensor current $I_{4,S}$ is a short circuit current, this approach is not applicable.

Striggow and Dankert ([14]) mention the voltage conversion using an inverting amplifier. This is also used by Kang Hui *et al.* ([17]) and depicted in Figure 18.

The resistance R_M in the feedback-loop can be tuned to increase the signal voltage U_{R_M} to use the full range of the ADC.

ADC
ADCs convert an input voltage into a digital signal. The requirements for the DAC result from the signal to be measured and the required resolution. The time varying signal

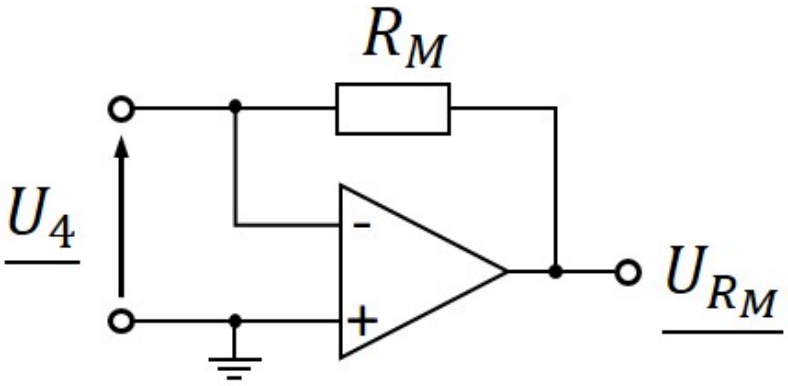

Figure 18: *Virtual ground concept using inverting amplifier*

requires a sample and hold element ([29, p. 1051]). Since the resolution required in the application is not defined. Therefore an equal size to accuracy is chosen. This requires according to [5, p. 152] a resolution of the ADC of

$$n = log_2\left(\frac{FSR}{LSB}\right) = log_2\left(\frac{75\ mS/cm}{0.0345\ mS/cm}\right) = 11.08\ Bit \rightarrow 12\ Bit. \tag{29}$$

Tietze ([29, p. 1032- 1053]) considers different types of AD converters in terms of operation, speed, and accuracy. ADCs using the parallel method ([29, p. 1035]) and the dual-slope method ([29, p. 1042]) are not considered because their resolution is too low. The 12-bit pipelined converters presented in [29, p. 1038] have a power dissipation of min 85 mW at sampling rates from 80 MS/s. 12-bit ADCs using the weighing method are listed with power dissipations of min 2 mW and sampling rates from 500 kS/s ([29, p. 1040]). Besides the sampling rate and the power dissipation, the aperture jitter is essential. This leads to a measurement error, since equidistant samples can no longer be assumed ([29, p. 1051-1052], [5, p. 137-139]). According to [29, p. 1052], for the permissible aperture jitter Δt_A, the following applies for a sinusoidal voltage with amplitude $\hat{U}$

$$\Delta t_A = \frac{U_{LSB}}{\hat{U}\omega_{max}} = \frac{U_{LSB}}{\frac{1}{2}U_{max}\omega_{max}}. \tag{30}$$

The virtual ground concept (Figure 18) allows theoretic infint gain on converation of current to voltage. Preceding the following chapter on circuit design, the reference value of 2.5 V is introduced here. This voltage represents the voltage of a reference voltage source. In terms of the requirements for the measurement circuit at a maximum signal amplitude of 2.5 V at 10 kHz frequency, a maximum jitter of a 12-bit ADC is

$$\Delta t_A = \frac{U_{LSB}}{\frac{1}{2} U_{max} \omega_{max}} = \frac{2.5\ V \cdot \frac{1}{2^{12}}}{\frac{1}{2} \cdot 2.5\ V \cdot 10e3\ Hz \cdot 2\pi} = 7.7\ ns. \tag{31}$$

Conclusion
The acquisition of the measured value requires a 12-bit ADC converter with a sample-and-hold element. Considering the accuracy and the frequency of the measurement signal, a maximum aperture jitter of 7.7 ns is permissible. Pipeline converters, as well as the weighing method, are available as the underlying method for the ADC. Due to the comparatively lower power weighing method based, ADC is preferable.

3.3.4 Data Processing

The next step is to determine the information about the conductivity from the collected data. Sensor current $I_{4,S}$ and water resistance R_w are proportional (Equation (16)). The intuitive approach of a peak-to-peak measurement is prone to noise. To reduce the effect of noise, which is not known at this stage, evaluating the sensor current in the frequency domain is sufficient. This is advantageous since the exciting voltage is of known frequency. The amplitude of the frequency coinciding with the frequency of the excitation contains the necessary information for determining the conductivity. A constant offset of a periodic oscillation transformed into the frequency domain is a Dirac pulse at the origin. It thus does not influence the amplitude of the frequency transformed oscillation [9, p. 345].

For the frequency transformation of discrete-time signals, the discrete Fourier transform (DFT) with its computationally efficient implementation in the Fast Fourier transform (FFT) is to be applied [9, p. 258].

The DFT is a derived form of the Fourier series of periodic sequences, and thus periodic signals can be correctly mapped to the frequency domain [9, p. 262]. The transformation of non-periodic signals (for example, noise) as well as of periodic signals of frequencies not covered by the window spanned by N data points, resulting in leakage effects [9, p. 262]. The spectrum of the FFT is composed of n individual data points. Using the correlation

$$f = \frac{n}{NT} = \frac{n f_s}{N} \tag{32}$$

given in [9, p. 259], the frequency is to be extracted from the value of n and the time interval $T = 1/f_s$ between two sample points. For this N data points are processed, transformed

$$X[n] = \sum_{k=0}^{N-1} x[k]e-j2\pi\frac{kn}{N} \tag{33}$$

yield. The amplitude of $X[f]$ is determined by

$$X[f] = \frac{1}{NT}\sum_{n=-\infty}^{\infty} X[n]\cdot\delta\left(f-\frac{n}{T}\right), \tag{34}$$

given in [9, p. 259][3]. From the restriction on the coverage of entire periods, it follows that the sampling frequency f_s must be an integer multiple of the oscillation under study. The Nyquist theorem requires a minimum sampling rate of $f_s \geq 2f$. The number of generated data points is

$$N = x\frac{f_s}{f}. \tag{35}$$

The factor x is the number of periods of the fundamental signal considered. Different combinations of x and f_s result in the same numerical value. Reducing the number of samples N reduces computational resources to perform FFT. From Equation (16) and Equation (13) it follows that the conductivity is given by the ratio

$$\kappa = \frac{I_{4,S}}{U_1}N_1N_4k_{\text{cell}}. \tag{36}$$

Assuming a constant amplitude of the primary voltage U_1, the conductivity is obtained as the product of the amplitude of the measuring current $I_{4,S}$ and a sensor constant k_{sensor} according to

$$\kappa = \frac{I_{4,S}}{U_1}N_1N_4k_{\text{cell}} = k_{\text{sensor}}I_{4,S}. \tag{37}$$

However, drift on the input voltage amplitude can not be neglected. An observation of input voltage according to the current observation is mandatory.

3.3.5 Handling and Communications

According to the list of requirements, conductivity levels in the range of 75 mS/cm and 2 mS/cm are expected that have a resolution of 0.0345 mS/cm. Twelve bits are sufficient

[3] At the end of the book page

to represent the range of conductivity values (Equation (29)). The smallest suitable data type for floating-point numbers is float.

UART implements data communication. It uses one to two stop bits for data transfer synchronization. The number of transferred data bits is variable and ranges from five to eight Bits. Sending different data types via UART requires converting subroutines to split the data into a UART data package size. Common data types are one or multiple Byte in size. Therefore data transfer uses eight Bits for data. Therefore, a data transfer of 32 Bit floating-point numbers requires four data transfer events. Sending sampled data of 12 Bit size requires two data transfers. The data transfer rate depends on the baud rate. Table 8 shows different data transfer rates for a default baud rate of 9600 and the maximal standard baud rate of 230400 of *CoolTerm*, a serial port terminal application. The formula to calculate the required baud rate for the described transmission[4] is

$$\text{Baud} = (1+8)\,\frac{\text{data type size (Byte)}}{2}\text{data items.} \tag{38}$$

Since the minimum sampling frequency for a 10 kHz signal is 20 kHz, UART is not capable to stream sampled data in real-time.

Table 8: *List of possible data transfer rates using one stop Bit and eight data Bits*

Baud rate	1 data transfers (1/s)	2 data transfers (1/s) (16 Bit data items)	4 data transfers (1/s) (32 bit data items)
9600	1066	533	266
230400	25600	12800	6400

3.4 Final Concept

The final concept represents a summary of the preceding considerations. Individual parameters are adapted depending on the requirements of selected components in the implementation context of the following chapter.

The final concept (Figure 19) consists of a module for signal generation, which is implemented based on the AWG. The TICS consists of transformers with ten turns each, the cores made of the material N87 with the dimensions 25.3x14.8. Excitation is at 10 kHz. Shielding of the cores against crosstalk is not mandatory due to the minor effect.

An inverted amplifier converts the sensor current into a voltage. The resistance of the feedback loop amplifies the output signal to the full range of the ADC. The acquisition

[4] One stop Bit + eight data Bits

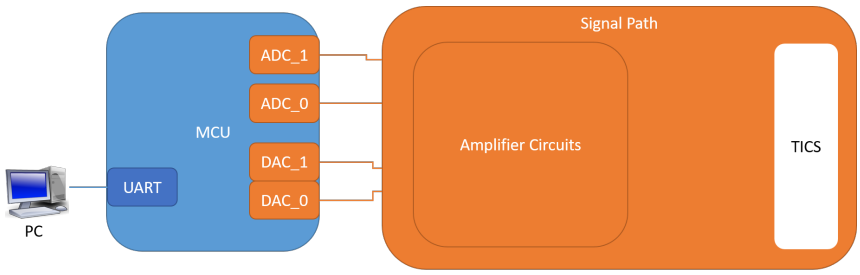

Figure 19: *Block diagram of final concept discussed in this section*

of the measurement voltage requires an ADC with sample-and-hold, preferably based on the principle of the weighing method. Its aperture jitter should not exceed 7.7 ns.

Data acquisition and evaluation requires sampling rates that are a multiple of the excitation frequency. Data is transmitted via a UART interface in a configuration of eight data bits and one stop bit. Depending on the requirement on data transmission, a suitable baud rate must be selected.

4 Implementation

This chapter describes the implementation of the conductivity sensor. Section 4.1 describes the selection of the components as well as the design of the circuit and the board layout. In Section 4.2 the program structure and the functionality of the sensor is described. Finally, Section 4.3 verifies the functionality.

4.1 Physical Sensor Hardware

The MCU, whose fundamental task is coordination and data evaluation, is provided by the institute; it is the SAME51G18A-MU. The chip is designed to run on 1.71 V to 3.63 V at -40 °C to +125 °C. It is equipped with two ADC channels which are capable to sample up to 1 MSPS [23, p. 1431]. The ADCs resolution is 12 bit in single mode and 11 bit in differential mode [23, p. 1435]. The jitter is listed to be 0.42 ns [23, p. 1817] (DFLL48M used as clock source). A 12 bit DAC unit with two channels able to operate in differential mode is implemented on the chip. The I/O pins are designed to 2 mA in normal mode operation and 8 mA in 'stronger mode' [23, p. 825, 1795].

The ADCs implemented on the chip meet the requirements listed in Equation (29) and Equation (31) for the ADC to be used. Since the MCU also has integrated DACs, additional components are not needed here either. The electrical circuit design starts with the voltage reference and is described in the following subsections.

As mentioned above, it is not possible to specify the cell constant exactly. Therefore, a cell constant of one is used in this section, as previously in the concept generation section. From looking at Equation (13), it is clear that a cell constant greater than one is to be expected.

4.1.1 Voltage Reference for ADC and DAC

A constant voltage supply via the drifter buoy is not guaranteed. The robustness of the voltage reference is important for the DAC and ADC to provide reliable data for subsequent calculations. Trailokya and Zamora present voltage references for various use cases in [30]. Recommended for a 12 bit DAC application are the *REF31*, *REF33*, and *REF4132* voltage references. Of these, *REF4132* was chosen due to good availability in sufficient quantities at the time of material procurement. The available voltage references of the component range from 2.5 V to 5 V. The MCU [23, p. 1800] datasheet lists a reference voltage for the ADC in the range of 1 V to $VDD_{ANA}-0.4$ V. Since a supply voltage of VDD_{ANA}=3.3 V is desired, a 2.5 V voltage reference is chosen.

4.1.2 Dimensioning TICS

Noise on the TICS wires are not known, so a voltage amplitude of 1 V is provided at the primary coil for an initial embedded prototype. Kandur [16] and Kang Hui [17] used 300 mV and 600 mV, respectively. The short-circuit current $I_{4,S}$ flows through resistor R_M (Figure 18) to generate the measurement voltage to be detected by the ADC. The resistor R_M is designed to convert the maximum expectable signal to the reference voltage U_{Ref} of the ADC

$$R_M = \frac{I_{4,Smax}}{U_{Ref}}. \tag{39}$$

Using Equation (39) and the relationship between voltage and current and the relationship between current and power, it follows

$$P_{R_M} = \frac{I_{4,Smax}^3}{U_{Ref}}. \tag{40}$$

According to Equation (40), a reduction of $I_{4,S}$ leads to a reduction of power dissipation in the amplifier circuit. Therefore, the short-circuit current is limited to 10 mA. The nominal diameters of the cores are 25.3x14.8 mm (Figure 17), their length is based on Kandur [16] and is 10 mm (uncoated, [27]). Considering coils with the same number of windings lowers the unit cost of the coils, since only one design is required for the TICS. Figure 20 displays the magnitude of the short-circuit current falling below the 10 mA mark for the first time at $N_1 = N_4 = 26$ (Figure 21 shows that a k factor = 1 is relevant for the maximum short-circuit current.). The maximum current at the primary coil for the determined k-factor of 0.945 is rounded I_1=15 mA (Figure 22).

4.1.3 Gate Driver and Measurement Circuit for TICS

The required amplitude of the TICS exceeds the technical specifications of the I/O pins of the MCU (2 mA, 8 mA in 'stronger mode' [23, p. 825, 1795]). An operational amplifier as impedance transformer [19, p. 432] contributes the required current. Operating the DAC in differential mode suppresses digital noise on the outputs of the DAC. The measurement range, which is twice as large as that of single-ended operation, reduces the influence of other noise on the output signal by half. The use of the differential DAC requires that the operational amplifier act as an inverting amplifier in addition to its function as an impedance transformer. Kester [18, p. 5] lists a suitable circuit for the presented case. The circuit shown (Figure 23) is adapted for the application.

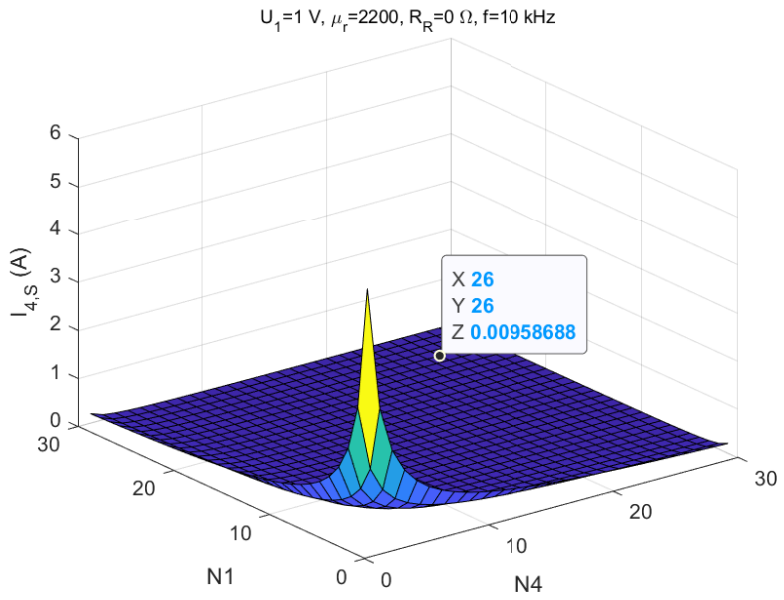

Figure 20: *Dependency of sensor output current $I_{4,S}$ on core turns N_1 and N_4*

Resistance to ground limits current flow when voltage is generated. The maximum voltage is 1 V as mentioned at the beginning of this section. For a maximum allowed current of 2 mA, a resistor of $R \geq 500\ \Omega$ is required. Parallel connection of two resistors requires

$$R_1||R_2 = \frac{R_1 \cdot R_2}{R_1 + R_2} = R_1 \frac{R_2}{R_1 + R_2} = R_1 \frac{R_2}{R_2\left(\frac{R_1}{R_2} + 1\right)} = R_1 \frac{1}{\frac{R_1}{R_2} + 1}. \tag{41}$$

The $R_{2,1}$ and $R_{2,2}$ resistors of the Figure 23 are combined into R_2 for simplicity. If $R_2 \leftarrow \infty$ runs $R_1||R_2 \leftarrow R_1$. From the condition of parallel resistance $R_1||R_2 \geq 500\ \Omega$ the possible combinations shown in Table 9 result with Equation (41).

Table 9: *Combinations of R_1 and R_2*

$R_1(\Omega)$	min$R_2(\Omega)$	source of R_1
511	23k23	E48
536	7k45	E48
549	5k6	620 E24 - 5%
590	3k3	E48
620	2k6	E24

The R_1 resistor of the E24 series is used. The required minimum resistance $R_2 = 2.6\ k\Omega$ is implemented by two equally sized resistors $R_{2,1} = R_{2,2} = 2.7\ k\Omega$. The boundary case

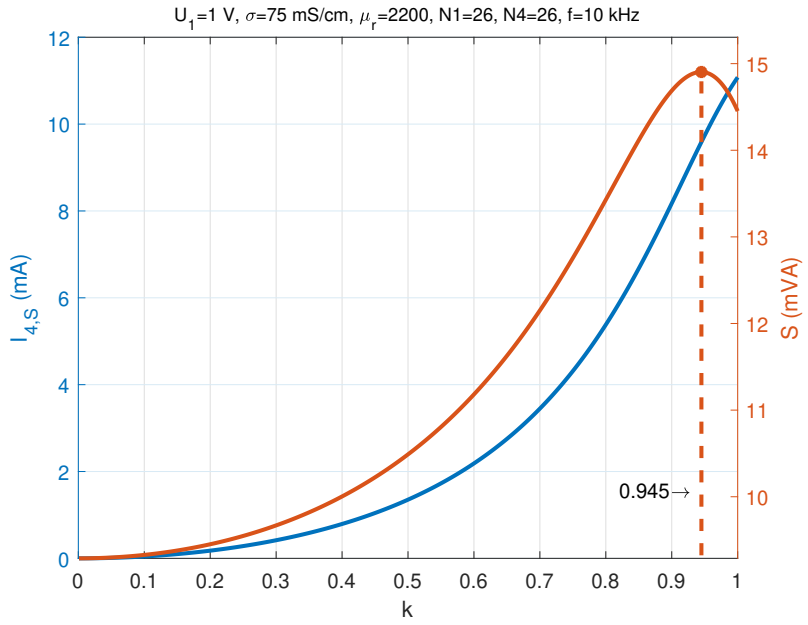

Figure 21: *k-factor for new sensor design*

consideration

$$500 \geq R_1 \cdot 95\% \frac{1}{\frac{R_1 \cdot 105\%}{(R_{2,1}+R_{2,2}) \cdot 95\%} + 1} \tag{42}$$

results in a parallel resistance of 523 Ω. The capacitor is designed as a low-pass filter according to

$$f_{3dB} = \frac{1}{2\pi \cdot 2R_1 \cdot C} \Leftrightarrow C = \frac{1}{2\pi \cdot 2R_1 \cdot f_{3dB}}. \tag{43}$$

To allow excitation with higher frequencies, taking into account Nyquist (sampling theorem), the corner frequency f_{3dB}=200kHz is chosen. Value 1.3 is closest to the calculated value of 1.28 in the E24 series. The cutoff frequency of the filter is 197 kHz for the capacitance of 1.3 nF. Hence, the design supports excitation of up to 98 kHz.

The final element of the sensor amplifier is the OpAmp. Another one is located on the secondary side of the TICS. Using the same components lowers the individual part cost due to higher quantities, therefore the same component should be used in both cases. Adjusting the gain by R_M (compare Equation (18)) results in a potentially larger signal magnitude. The largest temporal change in a sinusoidal signal is at the turning point. A maximum signal with respect to the reference voltage of the ADC has an amplitude of 2.5 V. For a frequency of f=30 kHz (used by Kandur [16]), this results in a slew rate of

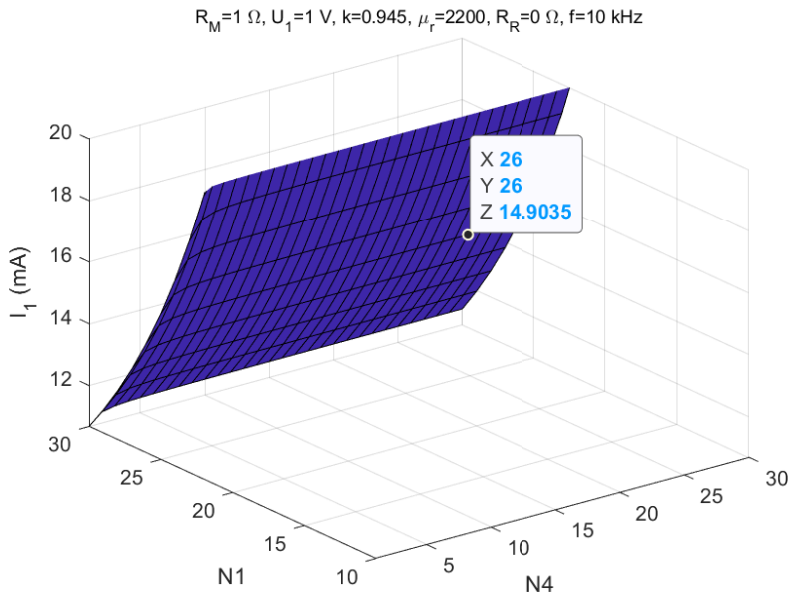

Figure 22: *Sensor input current I_1 for new sensor design*

471 kV/s. The op amp *MIC920* is the least expensive component available that meets the requirement.
The last element of the measurement chain not yet considered is the resistor R_M at the inverting amplifier. Ideally, the maximum applied measurement signal of $I_{4,S} \approx$10 mA (Figure 20) scales to the reference voltage V_{REF}=2.5 V by means of R_M. Noise disturbances with effect on the output signal are not known before the circuit is built. For this reason, an exact calcuation is not made. A resistor of the size 200 Ω from the E24 series approximates the requirement. In case of a deviation from the nominal size to 210 Ω due to tolerances, a buffer of U_{R_M}=400 mV exists. The short-circuit current $I_{4,S}$ has according to

$$I_{4,S\text{ puffer}} = \frac{U_{R_M\text{ puffer}}}{R_{M105\%}} = \frac{400mV}{210\Omega} \tag{44}$$

a puffer of $I_{4,S\text{ puffer}}$ =1.9 mA. These considerations assume a cell constant of unity. In order to select the ideal amplifier resistor for this application, the constant must be determined in advance by experimentation. With a higher cell constant k_{cell} decreases[5] the sensor current. This relation requires a resistor R_M greater by a factor of the cell constant.

[5] R_w increases by a factor of k_{cell}, so $I_{4,S}$ shrinks; Equation (16)

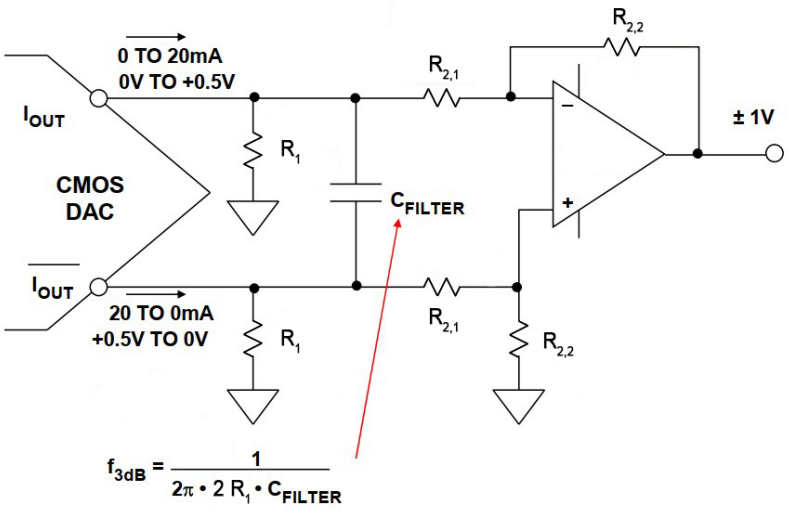

Figure 23: *Differential DC coupled output using a dual supply op amp by [18, p. 5]*

4.1.4 DC-DC Converter

5 V supply voltage is provided from the iMEK's buoy. A DC-DC converter converts this down to a supply voltage of 3.3 V. The operational amplifiers require bipolar supply voltages. The data sheet of the MCU [23, p. 1791] lists a maximum current requirement of 19.68 mA (configuration FDPLL 120 MHz). Together with the demand of the measurement circuit (2 mA at the DAC output, $I_{4,S}$=10 mA), a demand of < 50 mA is thus to be expected. With a safety factor of 2, the DC-DC converter has an output current of 100 mA. The *R1D-053.3-R* from *RECOM* meets this requirement.

4.1.5 Sensor Schema

The final schematic Figure 24 is color-coded into task areas. The systems involved in measurement acquisition are highlighted in orange. The differential DAC unit generates the exciting signal. The differential amplifier also functions as the current amplifier stage. From here, a first reference measurement path branches off to the ADC_0 unit. The other branch leads to the primary coil, through the ground the circuit of the first coil is closed. From the secondary coil the signal line leads to the inverting amplifier. This amplifies the measuring signal and converts it into a voltage which is converted by the ADC_1 unit. The voltage supply and its supply lines are marked in blue. The voltage reference (green) is connected to the VREFA port of the MCU and thus serves as reference for the ADC and DAC. Reyes is working on the implementation of communication via CAN [21]. Therefore, the communication is temporarily implemented via UART for test purposes.

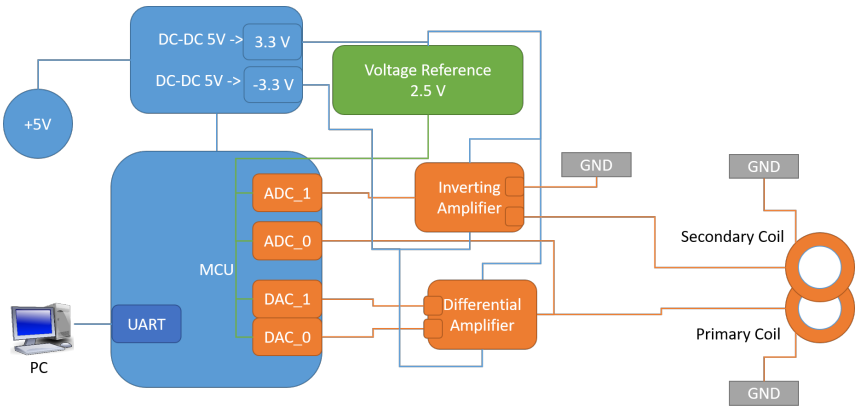

Figure 24: *Simplified block diagram of the embedded conductivity sensor*

4.1.6 PCB Design

The greatest challenge in circuit board design is the optimal positioning of the components on the smallest possible circuit board. Components with increased space requirements include the DC-DC transformer, the transformer coil, and the 10-pin headers. Placing these components on the edges of the PCB gains contiguous areas for the remaining components. Apart from the problem of optimal positioning, electrical interferences should be restricted where possible. Thus the coils maintain an additional distance of 10 mm from the circuits. An additional shielding[6] in the area of the coils provide shielding against mutual coupling.

The layout follows the design rules of [4] and [3] and the restrictions of the manufacturer *AISLER* [1]. Ground planes on both sides of the PCB are used to shield circuits. Multiple vias connect the ground planes distributed across the PCB to reduce potential differences between layers. The analog and digital ground are connected at the pin of the DC-DC converter (Figure 25) and otherwise separated according to [35, p. 824]. Vias shield sensor traces on both sides where possible. The signal traces are designed in 10 mils; the power traces start at 40 mil and branch into 32 mils.

ADC_0 and ADC_1 are connected with the pins 8 and 12 to the measurement traces and use pins 7 and 11 connected to analog ground as negative reference for differential mode operation.

Figure 26 shows the final PCB layout with the highlighted sections discussed in previous chapters. The non-highlighted components were added according to the requirements specified in the MCU datasheet schematic checklist [23, p. 1897-1908]. Layouts of the top and bottom layer are located in Section A.3. The dimension of the assembled PCB is 82.5 mm x 40.6 mm x 26 mm. The overall costs of he components is *lower* 20 €.

[6] connected copper planes on both layers

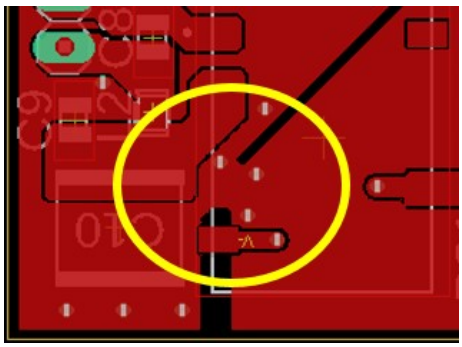

Figure 25: *Connection of digital and analog ground at the ground pin of transformer*

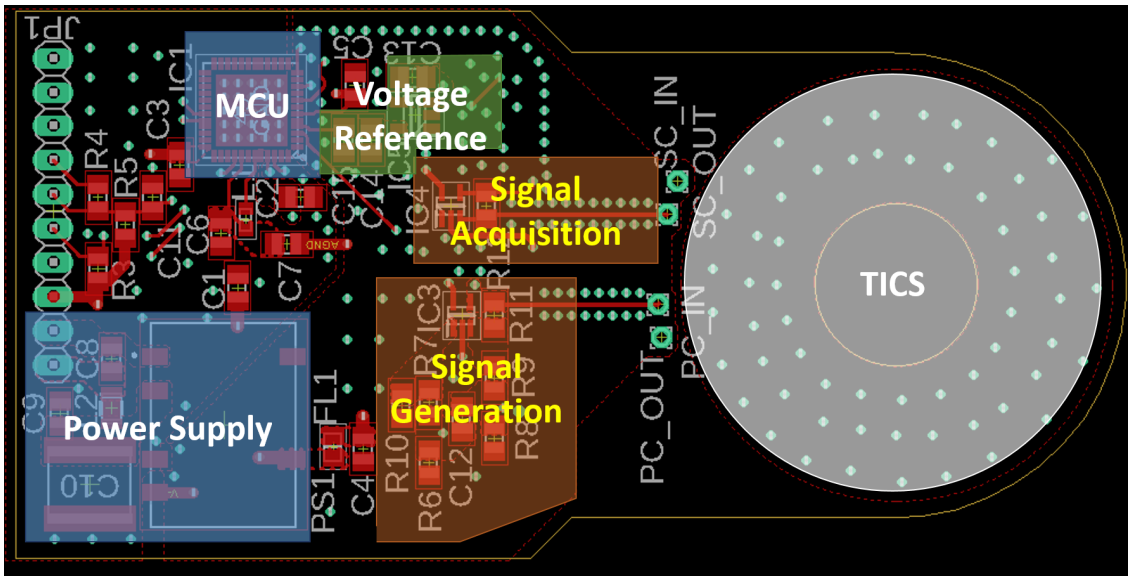

Figure 26: *Top side of final PCB layout*

4.2 Software Design - Principle of Operation

The following section is a theoretical consideration since a successful implementation in program code was not sufficient. Thus, no validation of the considerations made could be carried out.

The SAME51G18A-MU uses the Arm Cortex-M4 architecture. It can process digital signals ([26]) and is equipped with a floating-point unit ([23, p. 1]). The flash memory is 256 KB, has an EEPROM hardware emulation, and an embedded SRAM of 128 KB. As communication interfaces, the chip has a CAN instance [23, p. 19] and six serial communication interfaces (SERCOM). Both the CAN0 instance and the SERCOM5 instance connect to pins 31 and 32 of the MCU [23, p. 35]. Using these pins for UART or CAN creates a multi use PCB layout for test environments using UART and future applications with CAN.

The MCU also has a 32-channel event system for autonomous peripheral communication. Event generators and event users are specific to peripherals; multiple instances of event users and event generators are possible. Communication using the event system does not require CPU intervention or system resources such as bus or RAM. 32 Direct Memory Access Controller (DMAC) channels extend this functionality to memory accesses from peripheral devices. Transfer requests are triggered by transfer triggers[23, p. 340].

Finally, the MCU has a 32-bit real-time counter (RTC), which allows setting defined time intervals, e.g., for measurements. In the default setting, the main clock of the MCU runs at 48 MHz. The generic clock controller allows up to 12 generic clocks [23, p. 142].

4.2.1 Calibration Algorithm

The calibration requires three measurement points, two taken with known resistance values $R_{W,x}$ and one value for the conductivity. The sensor current $I_{4,S,x}$ is determined with an FFT analysis (Section 3.3.3). Using the two data points ($R_{W,1}$ | $I_{4,S,1}$) and ($R_{W,2}$ | $I_{4,S,2}$), the characteristic straight line equation

$$f(x) = mx + b \tag{45}$$

of the sensor is determined. The slope of the straight line is given by

$$m = \frac{I_{4,S,1} - I_{4,S,2}}{R_{W,1} - R_{W,2}} \tag{46}$$

is determined, the offset results in

$$b = I_{4,S,1} - mR_{W,1}. \tag{47}$$

Thus, the third measurement in a solution with known conductivity κ_3 yields the sensor current $I_{4,S,3}$, which is mapped to the resistance value $R_{W,3}$ via the characteristic straight line equation:

$$R_{W,3} = \frac{I_{4,S,3} - b}{m} \tag{48}$$

Using $R_{W,3}$ and the known value of conductivity κ_3, Equation (13) is used to determine the cell constant k_{cell}:

$$k_{\text{cell}} = R_{W,3}\kappa_3 \tag{49}$$

4.2.2 State Machine Sensor Module

The implementation of the sensor module is intended as a state machine. Tthe top level of the state machine consists of the states *UART Input*, *Calibration*, and *Measurement*. The RTC triggers the *UART Input* state on demand in a predefined cycle. From the state *UART Input* the RTC can be configured.

State Calibration
The state *Calibration*, becomes active after receiving the character '2'. It requests the input of two resistor values to calibrate the used resistor loops. After each input of R_W,x, the ADC and DAC turn on. Acquiring one and converting the readings provides the amplitude $I_{4,S,1}$ of the sensor current. After the acquisition, the DAC and ADC turn off. This process is repeated a second time. The characteristic straight line equation is determined as previously described from the data. Last, the conductance is sampled to measure the sensor current in a conducting solution. The cell factor k_{cell} calculated after this procedure, and the constants of the straight line equation m and b are stored in the EEPROM.

State Measurement
State *Measurement* becomes active after receiving the character '1'. ADC and DAC start and shut down after acquiring the data points needed for FFT. The acquired value $I_{4,S,1}$ is converted to a resistance value R_W,1 using the already known characteristic straight line equation[7]. The cell constant stored in the EEPROM is used to convert the value to a conductivity value.

4.2.3 UART Transfers

UART runs at a baud rate of 9600. Boolean variables track the status of RX and TX of the asynchronous UART. A corresponding interrupt routine sets the *'RX_Recieved'* boolean flag for the program code when a message is received. Reading the received data clears this flag. Similarly, sending data must be implemented to avoid data loss. A *'TX_ready'* flag tracks the status of the UART module. At the data transfer to the UART peripheral, the flag is set to 'true' and is not set to 'false' until the data transfer is complete. Since this flag must be checked before sending data to the peripheral, the MCU can run into a time-limited idle-loop.

[7] values for m and b are read from the EEPROM

4.2.4 DAC

A simulation in MATLAB *Simscape Electrical* of the TICS provides information on the optimal segmentation of the signal to be generated. The simulation showed that segmentation into 64 sections (6 bits) is sufficient for a continuous signal. The DAC runs at 640 kSPS to generate the 10 kHz sine wave with the specified resolution. According to [23, p. 1513], this requires a clock with a frequency of $f_{\text{GCLK\_DAC}}$ = 24·SPS=15360 kHz. As this frequency cannot be met by dividing the MCU clock of 42 MHz by multiple of two, a higher frequency clock is to be used. Using a higher frequency requires that an event controls the digital-to-analog conversion as mentioned in the datasheet ([23, p. 1512]). The second way of timing is time-controlled data transfer to the peripherals. The resources of the DMAC can be used for this purpose.

4.2.5 ADC

Comparable considerations apply to the ADCs. Reliable transformation of data points using FFT requires synchronization of DACs and ADCs (Section 3.3.4). Therefore, the ADCs must use the same clock as the DACs. According to the datasheet ([23, p. 1436]), a maximum sampling rate of N=590 kSPS is possible at a $f_{\text{GCLK\_ADC}}$=15360 kHz. According to Equation (35), this corresponds to a sampling frequency of 59 kHz at a factor of $x = 1$. Since it is not an integer multiple (Section 3.3.4), the conversion is event-driven. A clock with a frequency of $f_{\text{CLK\_EVENT}}$=40 kHz is suitable for this purpose, generating an event at each clock. The conversion results are pushed into the SRAM by a DMAC.

4.3 System Validation

4.3.1 Test of Shielding

The impedance and thus the effect of shielding on the mutual coupling is tested using the *IM 3570* impedance analyzer from *HIOKI*. For this purpose, a coil was first placed on each side of an unpopulated PCB and a 3D printed model (Figure 27).

The influence on the magnetic flux must be kept as low as possible. Therefore, the TICS hangs on the measuring clamps (Figure 28). The clamps on one side of the TICS were swapped to validate the experimental setup in terms of repeatability. The swapping resulted in three dimensions realignment of the TICS and clamps. This lead probably to changes in capacitance on the test setup since no shielded wires are used to connect clamps ad impedance analyzer.

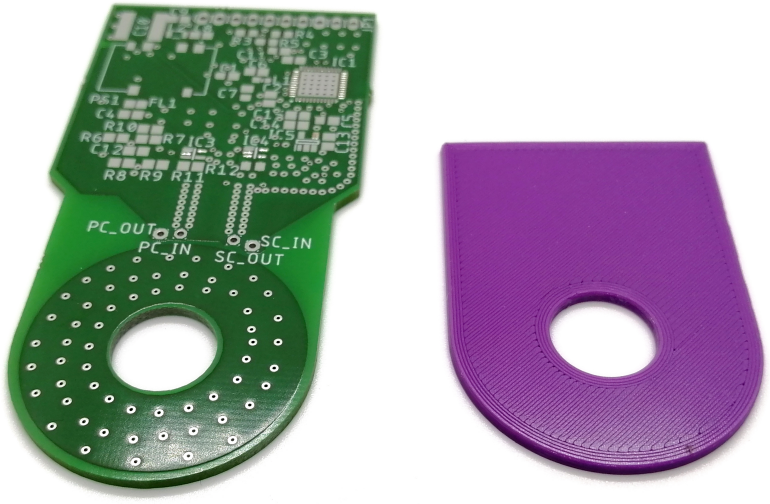

Figure 27: *PCB and 3D printed dummy*

The results of the impedance analysis with a sweep are shown in Figure 29 and Figure 30. As expected from before (Section 15 and Section A.7) the mutual coupling is of no concern, thus a shielding is not needed for excitation in the range of kHz.

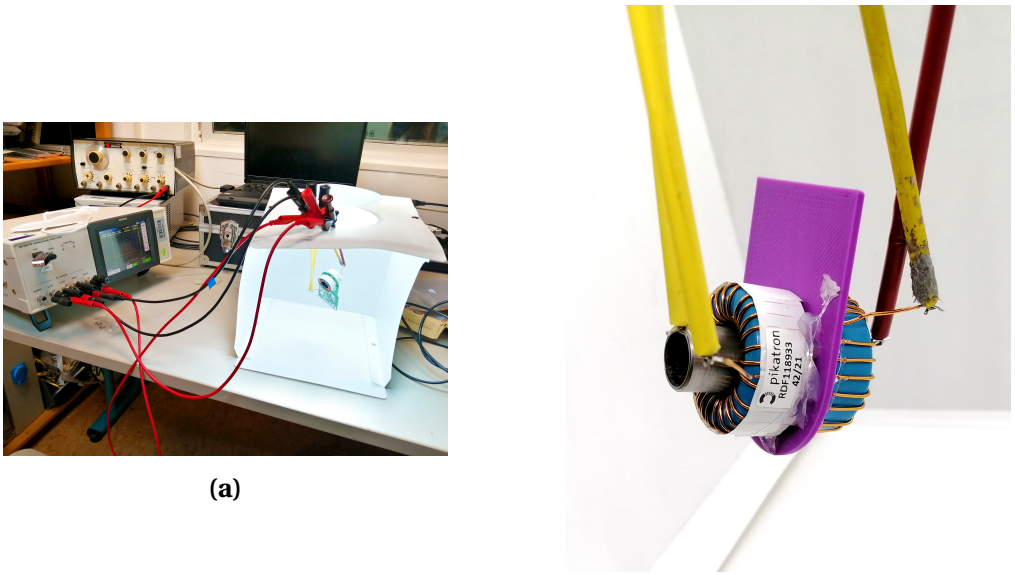

(a) **(b)**

Figure 28: *test setup for impedance measurement on TICS: setup **(a)**; TICS is held in the air by clamps **(b)***

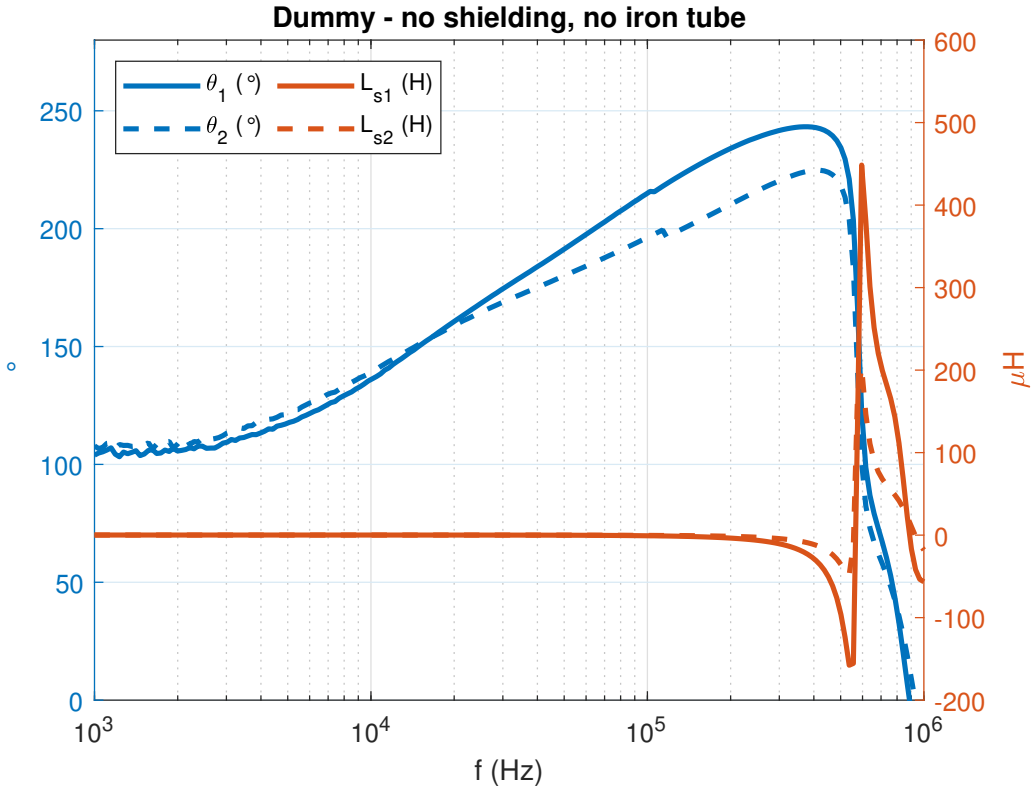

Figure 29: *Impedance profile of the TICS - no shielding*

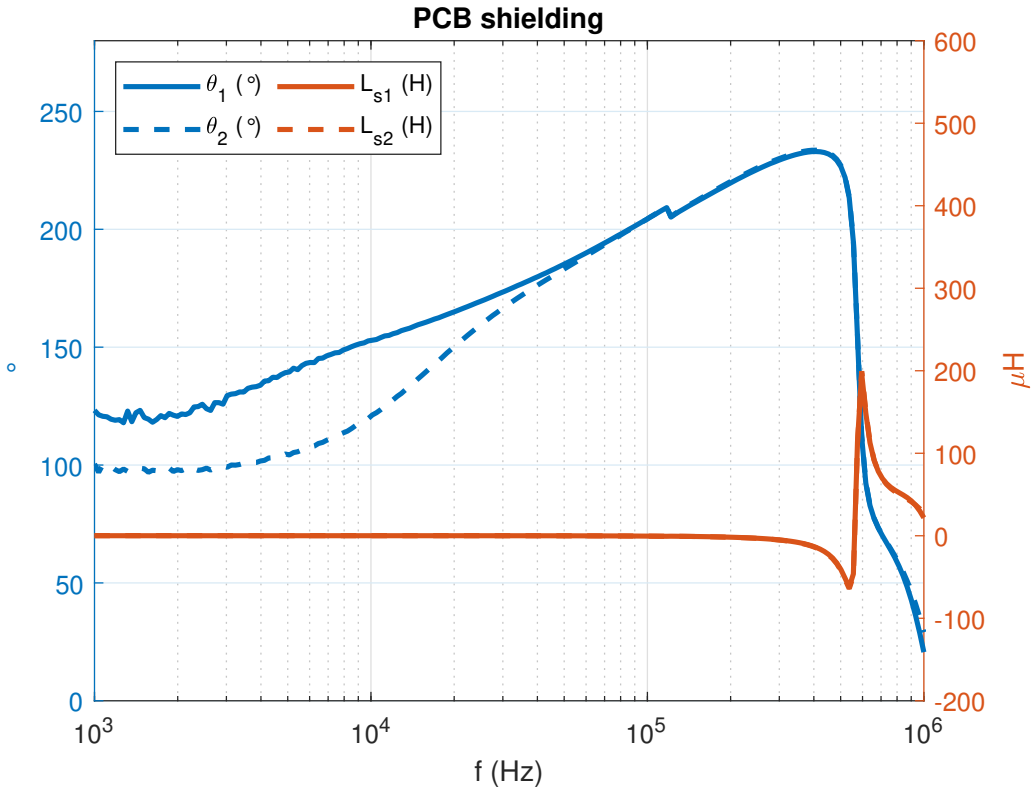

Figure 30: *Impedance curve of the TICS - PCB with shielding*

5 Results and Analysis

In this chapter, building on the results of the previous chapters, analyses are carried out and discussed. As mentioned before in Section 4.2, the implementation of the software was unsuccessful. Therefore, the following tests are limited to modules whose examined behavior allows relevant conclusions for the hardware implementation.

5.1 Test of Known Resistors

First, the operation of the TICS is probed for model validation. This is done using the TICS mounted on a printed circuit board previously described in Section 4.3.1. The magnetic flux previously described in theory is generated by applying a voltage to one of the two coils. A resistor of known size is wound once around the coils, passing through the centerlines of the coils. The various resistors carry a current equal to the equivalent resistance of water R_W in the equivalent circuit diagrams. Different resistance values are realized by shorting the conductor resistance to a toroidal coil or using different resistors. The primary coil is directly connected to the function generator *AFG 3021* from *Tektronix*, which generates the signal of 10 kHz with an amplitude of 1 V. The measurement signal is measured with the *RTB2004* Digital oscilloscope from *Rhode&Schwarz* and transferred to a PC via the USB interface for evaluation. Since this records voltages, conversion of the coil current via a terminating resistor of 1 MΩ is required. Figure 31 shows an example of the evaluation of such an experiment. Due to the experimental setup, a terminating resistor is required for the voltage measurement. The transfer function for this case is already given in Section 2.3 with Equation (15).

Using Equation (15) and the parameters known from the design, the system responses are calculated for the resistors used Table 10. The experimentally determined system responses are the maximum amplitudes in the frequency domain of the measured signals.

Table 10: *Resistors used for dry measurements*

#	value of resistance	value (measured)
1	wire	0.75^{8} Ω
2	47 Ω	49 Ω
3	470 Ω	488 Ω
4	100 Ω	100 Ω

The experimental and calculated system responses are shown in Figure 32. Smaller conductance values have the highest percentage deviation. Linearization of the mea-

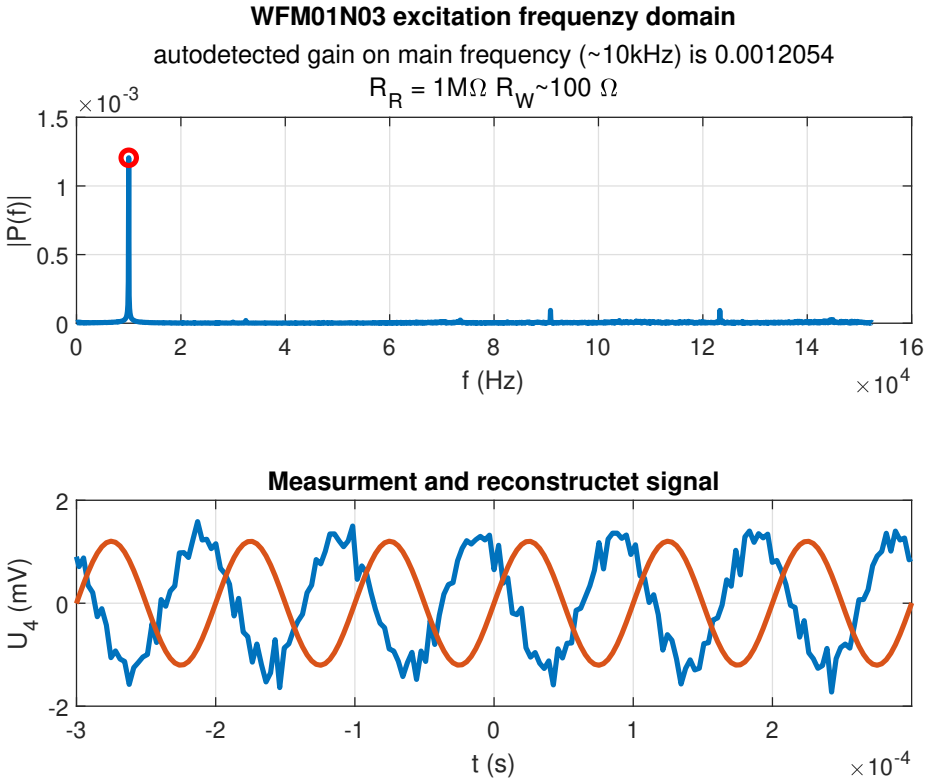

Figure 31: *Representation of the acquired signal in the frequency domain and time domain as well as a reconstruction*

surement points results in the straight line equation shown in Figure 33. A consideration of the system response for the measured case (resistance instead of virtual ground at the secondary coil) is given by Figure 34. The curve is approximately linear in the lower range of conductivity. Therefore, the straight-line equation presented earlier is not generally valid.

5.2 Determination of the cell constant

To ensure a sensor output of an amplitude detectable by the ADCs of the MCU, the cell constant k_{cell} must be determined. The procedure described in Section 4.2.1 is used for determination.Based on the previous investigations, the cell factor must be determined. This was already stated at the end of Section 4.1.3 as a critical factor for an accurate design. A more secure determination requires replacing the measurement circuit's amplifier resistor before the TICS can be cast. In addition to the previously used function generator and oscilloscope, the measurement setup is extended by a conductivity sensor. This causes periodic noise on the measurement signal recorded by

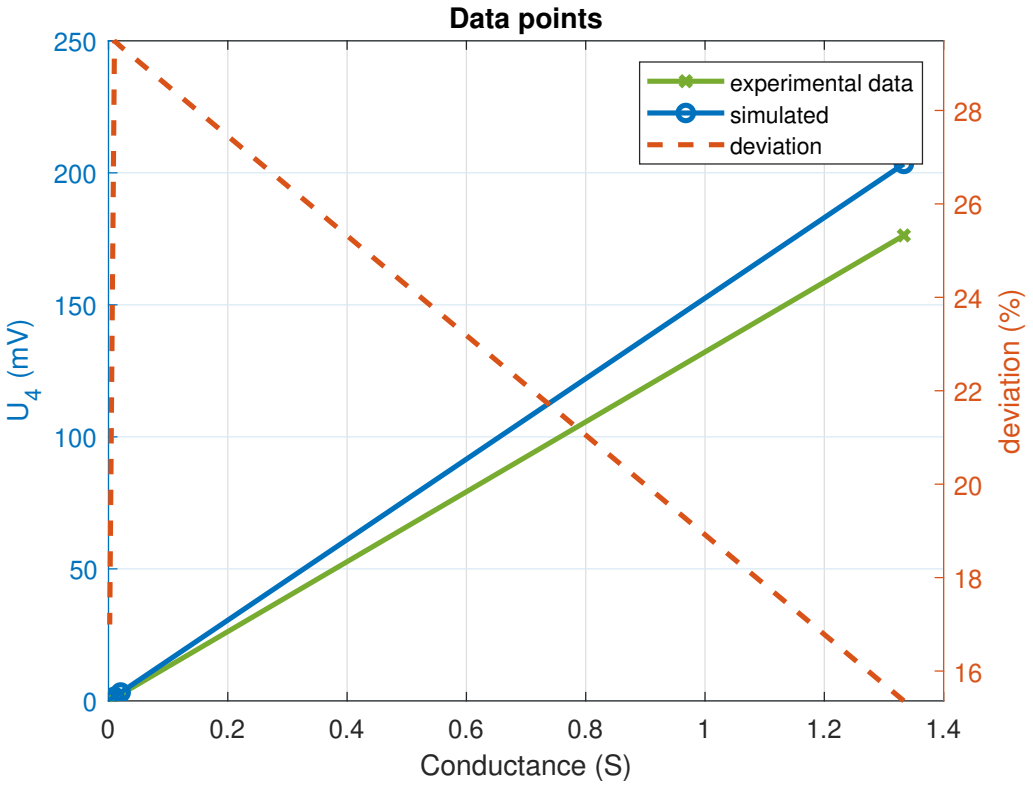

Figure 32: *Comparison of measured and simulated data*

the oscilloscope. To reduce the noise of the sensor, the external conductivity sensor is disconnected from the power supply for each data recording with the oscilloscope. The determination of cell constants requires measurement in a conductive medium. Before use, the sensor must therefore be encapsulated in a casing (Figure 35). The setup of the measuring circuit is identical to the previously performed measurement. Conductivity measurements are conducted in a tank with a capacity of about 60 l (Figure 36). The tank is filled with purified water, into which salt is stirred and between measurements.

The Figure 37 and Figure 38 show the output signal for a selection of conductivity values. The measurements made are also approximated by a characteristic curve (Figure 39). According to the relation in Equation (13), or

$$\frac{1}{G_W} = \frac{k_{\text{cell}}}{\kappa} \Leftrightarrow k_{\text{cell}} G_W = \kappa. \tag{50}$$

In the case of conductance, the cell constant k_{cell} is assumed to be linear. However, a comparison of the slopes of the approximated linear equations from Figure 33 and Figure 39 shows that this is not given exactly in this case. Nevertheless, the procedure is carried out as an illustrative example. First, the value of a voltage measurement of

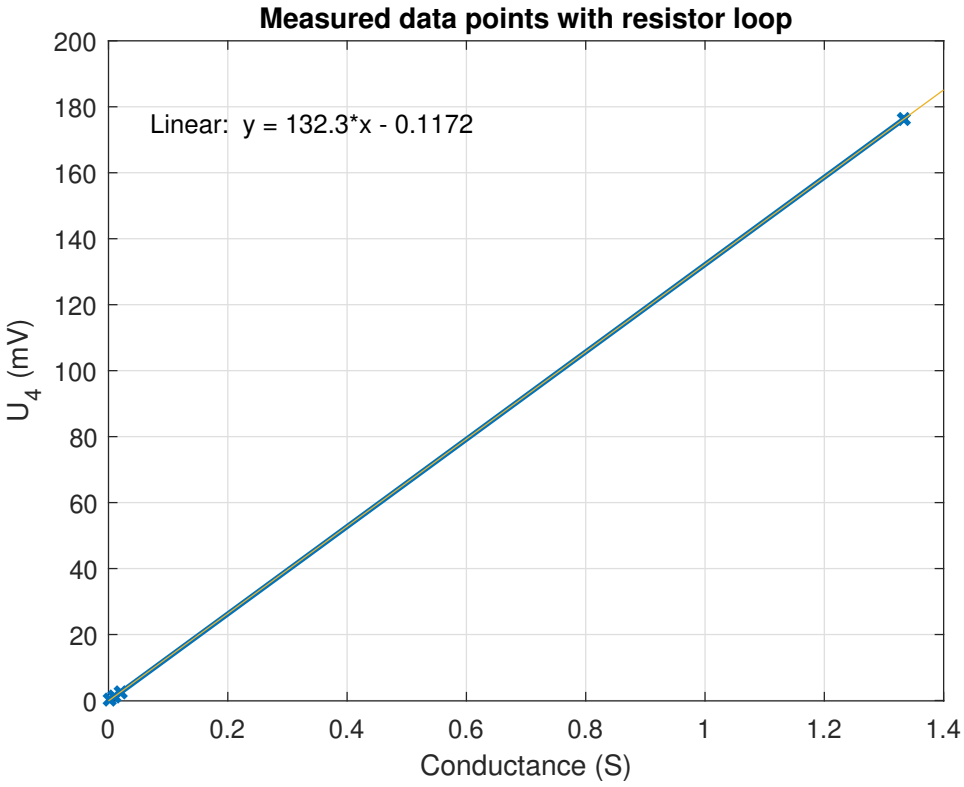

Figure 33: *Measured data with resistor loop*

the respective other measurement series is to be determined with the help of one of the linear equations. A conductance determined in this way is directly linked to the conductance belonging to the voltage value via the cell constant. In Table 11 measured values are displayed in the first two columns. The given conductance is determined via the straight-line equation given in Figure 33 for the voltage target value of U_4. From the transfer of G and κ, the listed cell constants k_{cell} are obtained The average is cell constant is 3.77 1/cm, the maximum difference is 1.1713 1/cm, which is 25.7 % of the maximum value. Possible causes for the difference are aliasing effects during sampling and Fourier transform. For example, in the FFT performed in MATLAB, the signal has peaks near 10 kHz, but never exactly at that frequency.

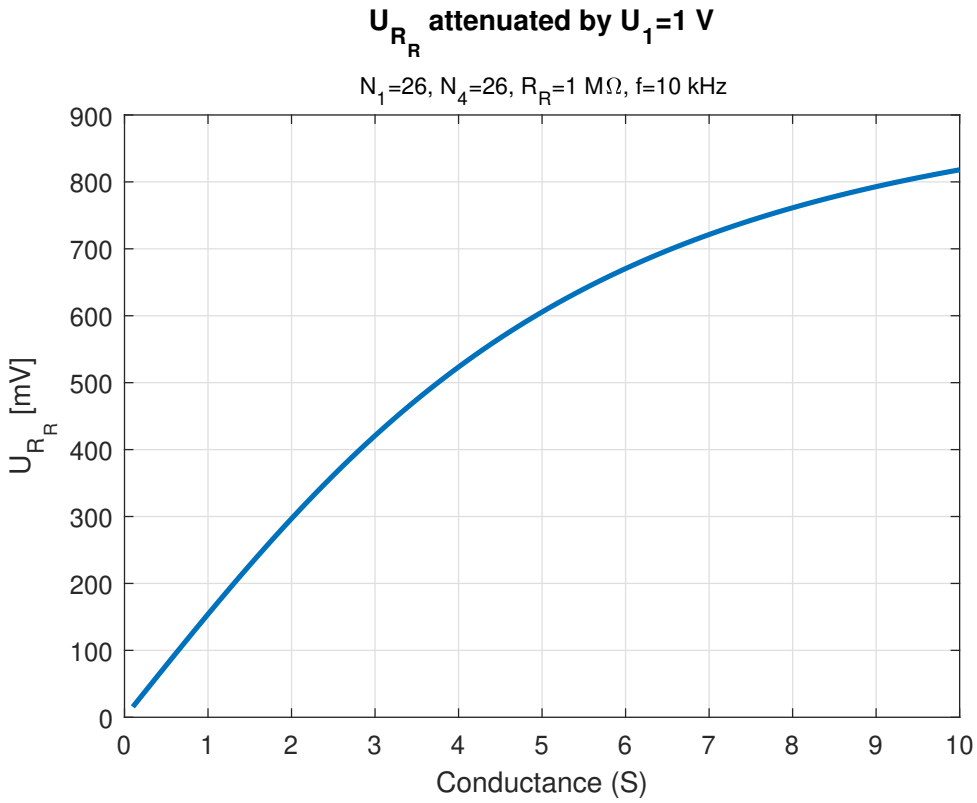

Figure 34: *Simulated behavior of system in test setup*

Table 11: *voltage and conductivity values from the series of measurements with the sensor potted in a water bath*

U_4 (μV)	κ (mS/cm)	G (mS)	k_{cell} (1/cm)
454.619	19.7	4.322139	4.5579
393.222	16.9	3.858	4.38
266.411	11.3	2.899554	3.897
192.584	7.93	2.341527	3.3866

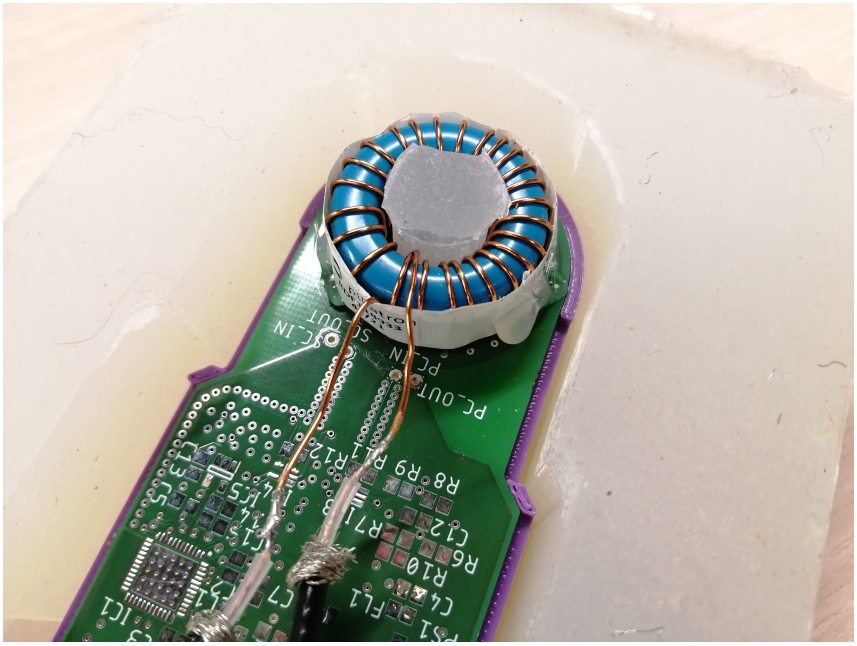

Figure 35: *TICS in a silicon molde*

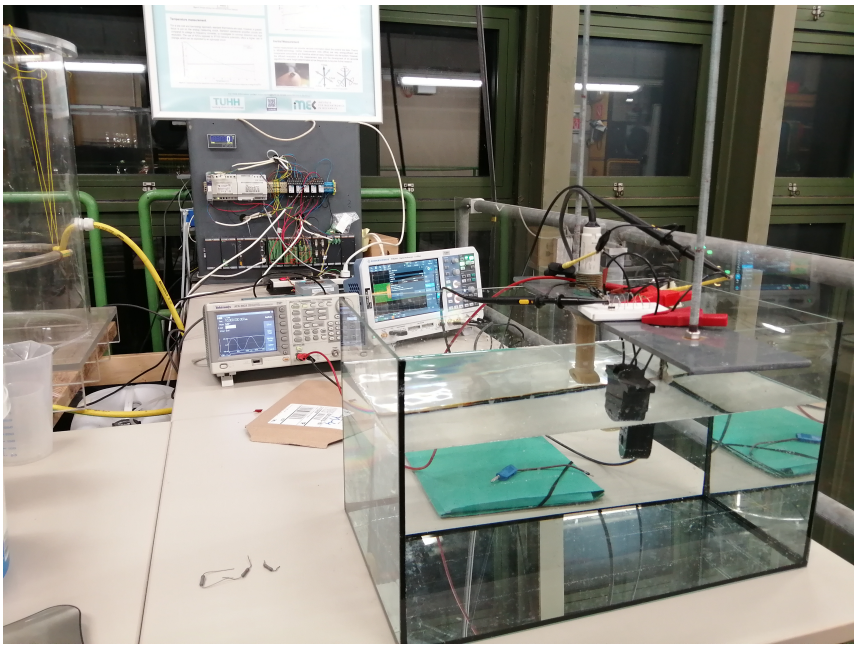

Figure 36: *Measuring setup for conductivity measurements*

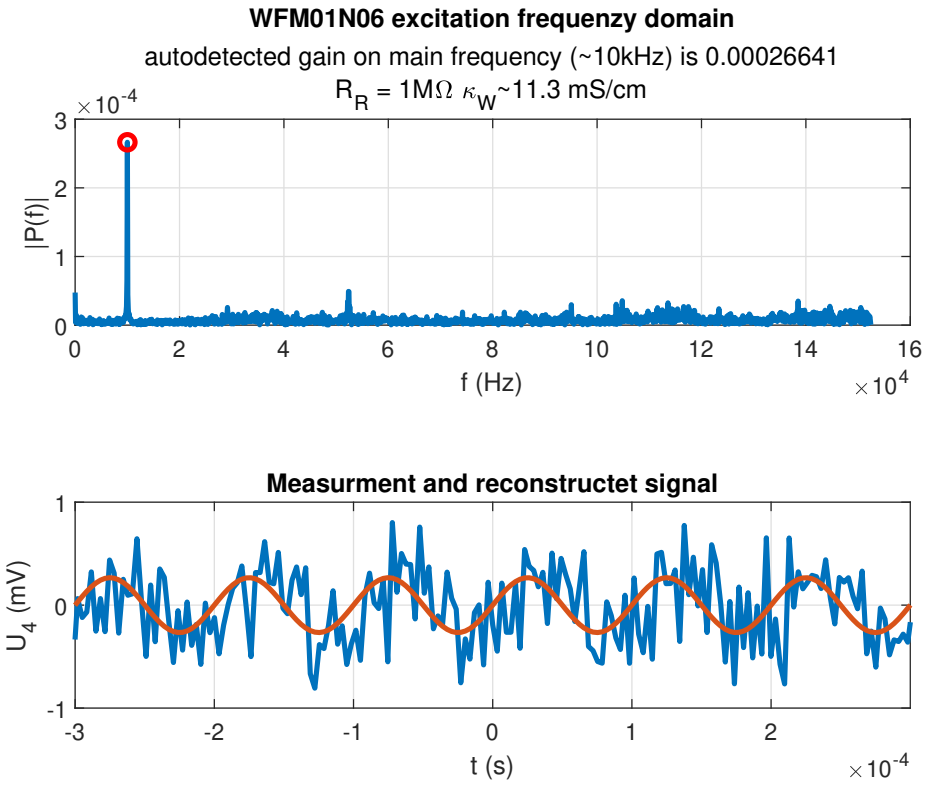

Figure 37: *Signal in frequency domain and time domain for 11.3 mS/cm conductivity*

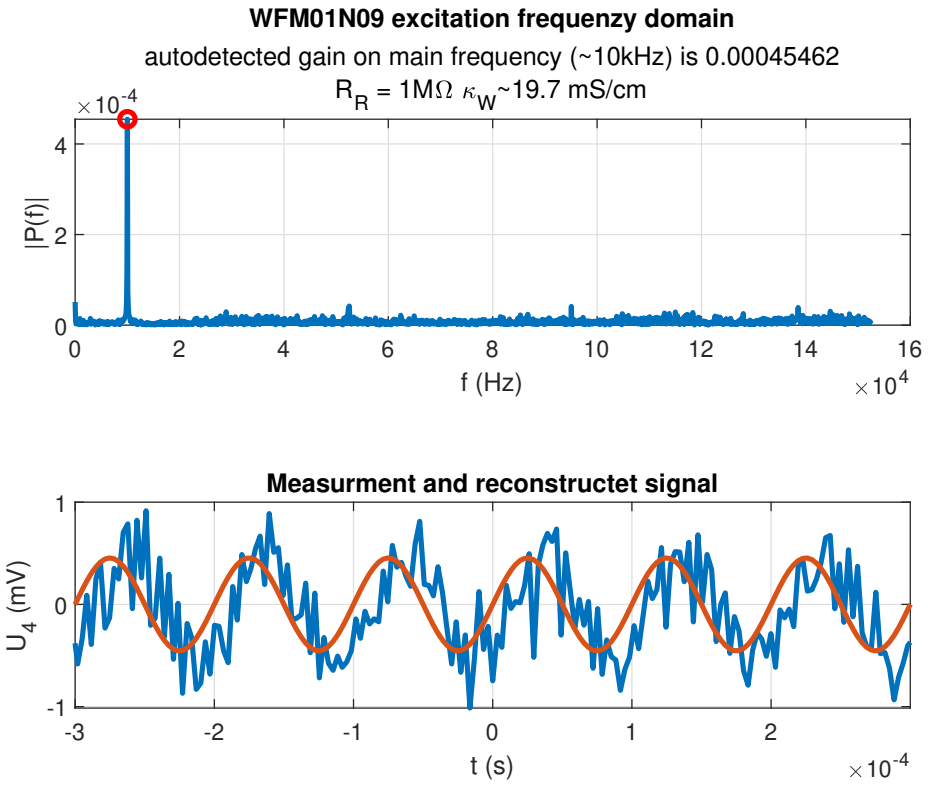

Figure 38: *Signal in frequency domain and time domain for 19.7 mS/cm conductivity*

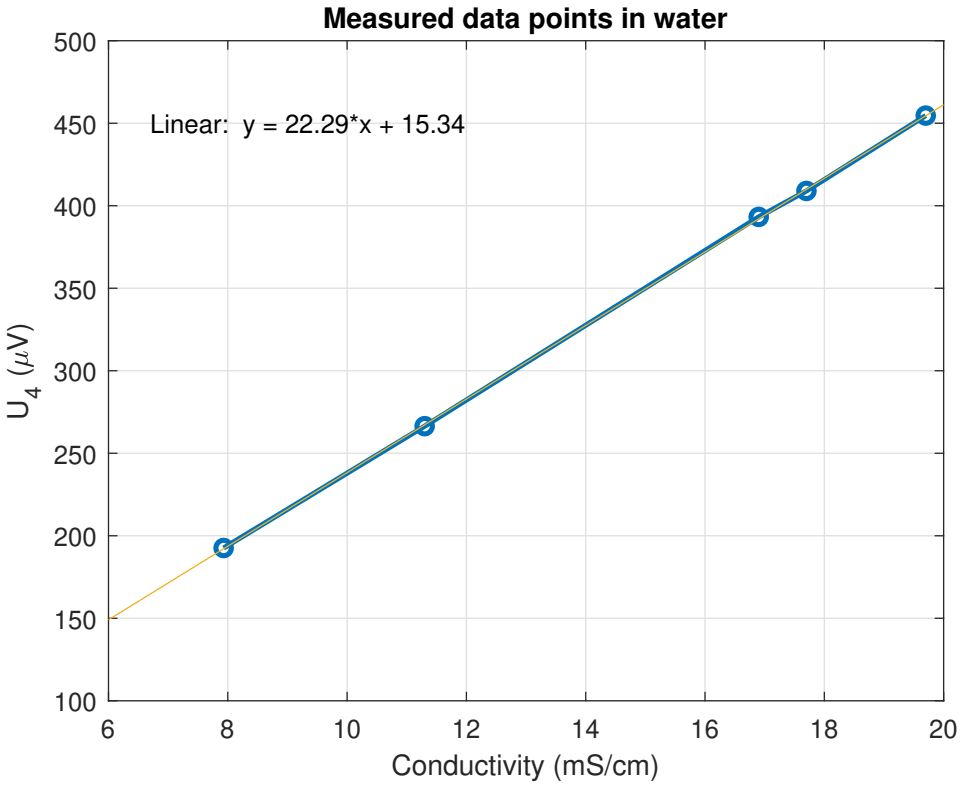

Figure 39: *Measured data using ionic solution*

6 Conclusion and Outlook

The aim of this master thesis was the development of a low-cost, low-power conductivity sensor for use in marine applications. Research on conductivity sensors suggested the double transformer type inductive conductivity sensor excited via a voltage of known frequency as a promising approach. A functional decomposition was conducted to split the main function into sub-functions of equal importance. Different approaches were discussed and future challenges for design and implementation were addressed. As such different parameters on the sensor design were optimized using simulations such as the number of windings, core size, and permeability. An integrated circuit is designed based on the SAME51G18A MCU and its peripherals. ADCs implemented in the MCU sample the signal at a multitude of its core frequency. The PCB is 82.5 x 40.6 x 26 mm^3 in size, the components used are <20 €. A housing and feasible mold are designed for long-term use. Using two DACs as a differential input source to reduce noise on the sensor, the sensing signal is sinusoidal, oscillating at 10 kHz. The received signal is amplified by hardware and sampled by the MCUs ADC modules. ADC and DAC use a voltage reference to further increase the stability of sensor signals. The received signal is then post-processed by software.

Due to shortcomings, the software of the MCU was not implemented. However, the software concepts for the measurement process are discussed. ADC and DAC need to operate in synced mode to reduce interference on the sampled data. The software design also addresses the process of sensor calibration.

Finally, the concept was tested on a small scale. The data acquired from TICS were successfully processed using FFT. An average cell constant of 3.77 was determined. A comparison with modeled data showed a behavior as expected. The performance of -30 % compared to model data is due to uncertainties in the model like the k-factor. However, a slight nonlinearity can be observed in the data. Thus a measurement in virtual ground configuration should be performed. The required sensor accuracy of 0.0345 mS/cm is not met if the 12 Bit ADC runs in differential mode; the accuracy is 0.0366 mS/cm, which is 21 µS/cm less than required. The integrated circuit needs to be modified according to the cell constant. Further investigations are required, as the calculated cell constants varied by 25 %.

In the future, software must be programmed for the sensor module. This should have top priority because only with the software the integrated circuit, especially the signal generation via DAC, and the sampling can be done. An ADC module with higher resolution is possibly necessary since component-related inaccuracies were not considered in detail. Concerning production in quantities > 10, the design and encapsulation process must be optimized for partial automation. For surface water applications, dip coating

could prove suitable here. Furthermore, the integrated circuit can be further optimized since no filter is provided on the secondary side. Such a filter can further improve the signal quality in terms of SNR.

A Appendix

A.1 Schematic

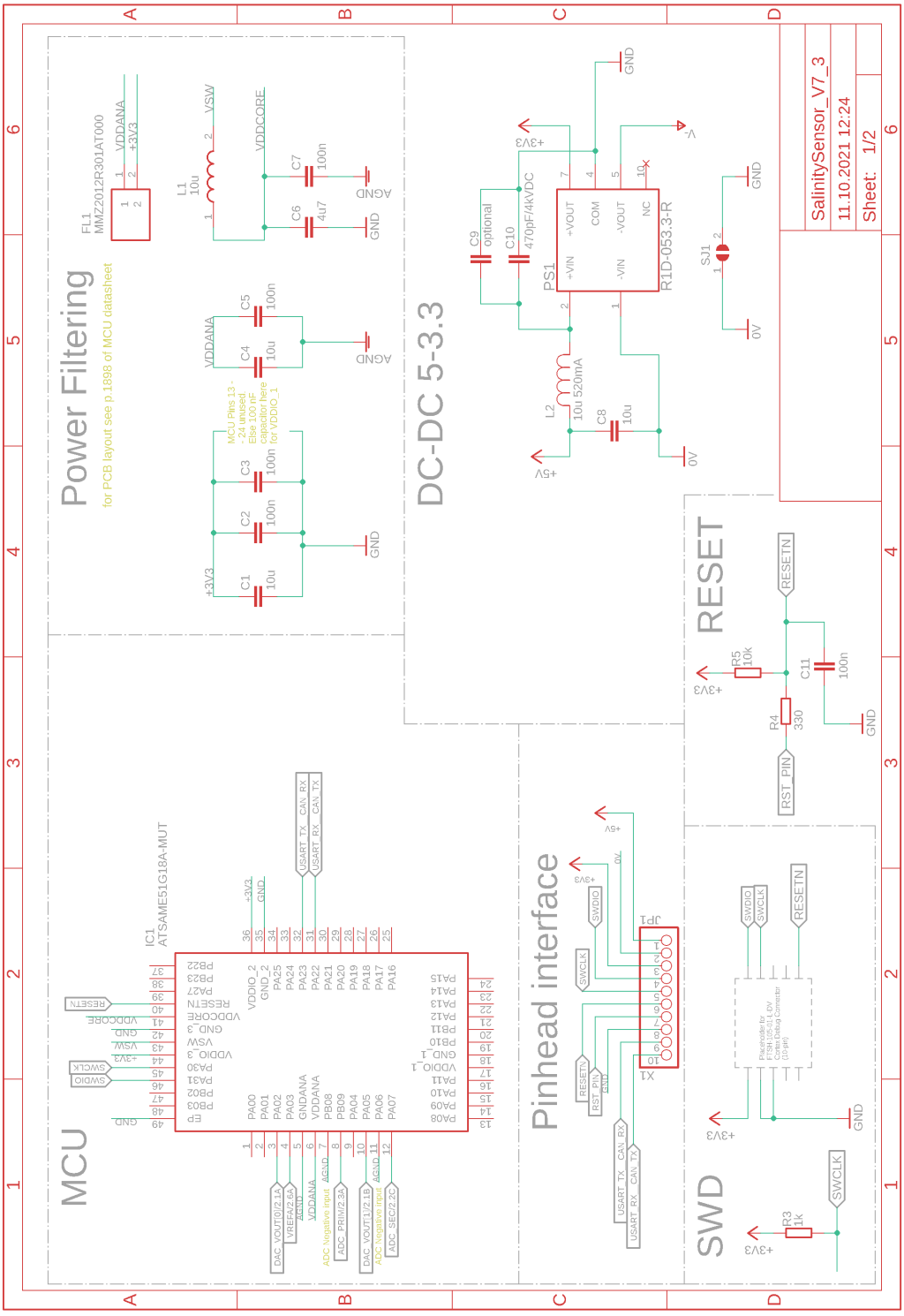

Figure 40: *Schematic page 1 - MCU and power supply*

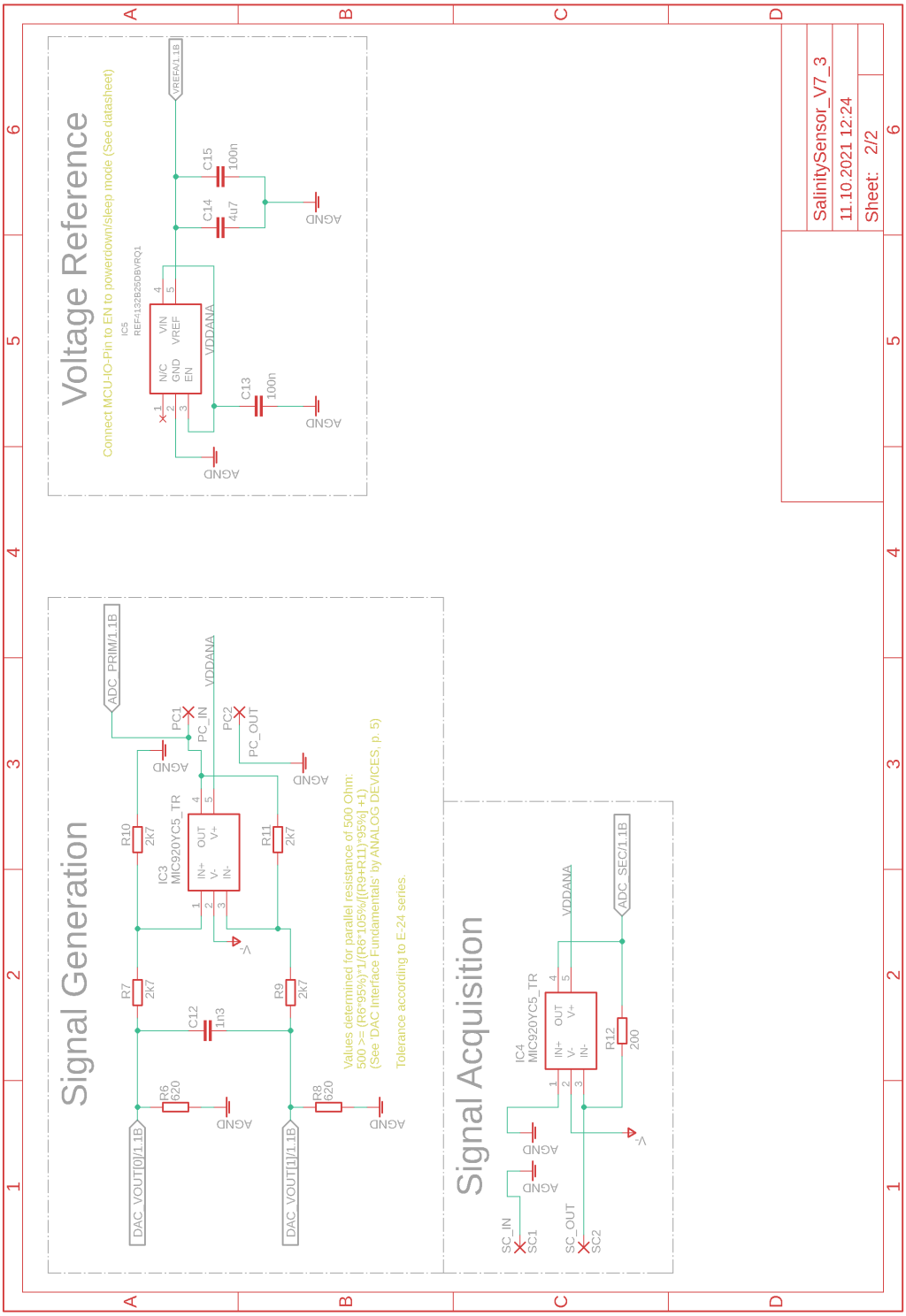

Figure 41: *Schematic page 2 - Measurement Circuit*

A.2 Bill of Materials

Table 12: *BOM*

Qty	Value	Parts	Description
1	470pF/4kVDC	C10	
1	1n3	C12	
7	100n	C2, C3, C5, C7, C11, C13, C15	
2	4u7	C6, C14	
3	10u	C1, C4, C8	
1	optional	C9	Alternative zu C10
1	MMZ2012R301AT000	FL1	5 Signal Line Ferrite Bead 0805 (2012 SMD)
1	ATSAME51G18A-MUT	IC1	
2	MIC920YC5_TR	IC3, IC4	
1	REF4132B25DBVRQ1	IC5	
1	X1	JP1	PIN HEADER
1	10u	L1	Fixed Inductors 3mA 2.55 Ω SMD
1	10u 520 mA	L2	Festinduktivität 10 uH maxDC 520 mA 500mOhm (80-L0805R100MDWST)
1	R1D-053.3-R	PS1	1 Watt SMD, isolated DC-DC-converter
1	200	R12	
1	330	R4	
2	620	R6, R8	
1	1k	R3	
4	2k7	R7, R9, R10, R11	
1	10k	R5	

A.3 Layout

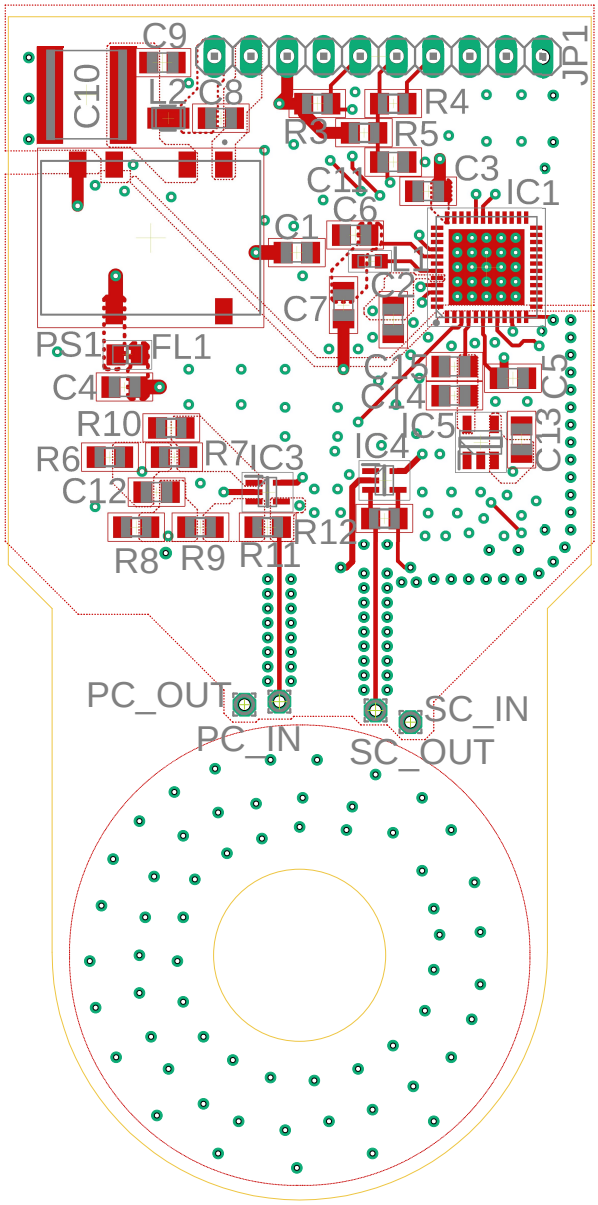

Figure 42: *Top layer*

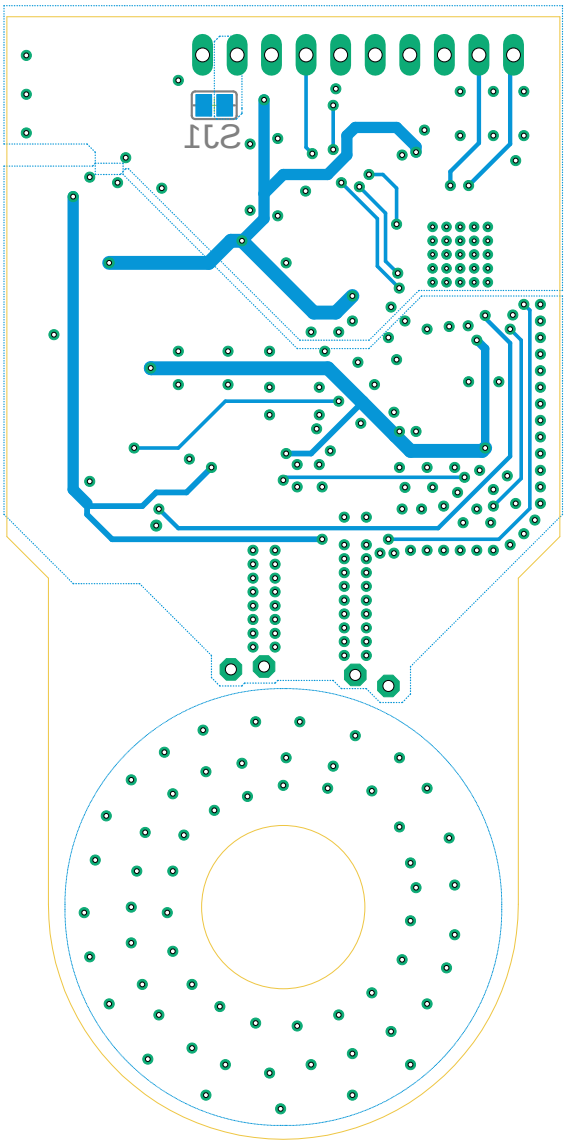

Figure 43: *Bottom layer*

A.4 Determination of Desired Sensor Resolution

The values of resolution in Section 3.1 were determined by using the MATLAB function 'gsw_C_from_SP.m' included in Gibbs-SeaWater (GSW) Oceanographic Toolbox on the TEOS-10 website ([28]).

A numerical deviation of S of the used function (Figure 44) shows the smallest value of the rate of change for high S and low T. A drop in S by 0.05 results in a change of 0.0345 mS/cm for κ.

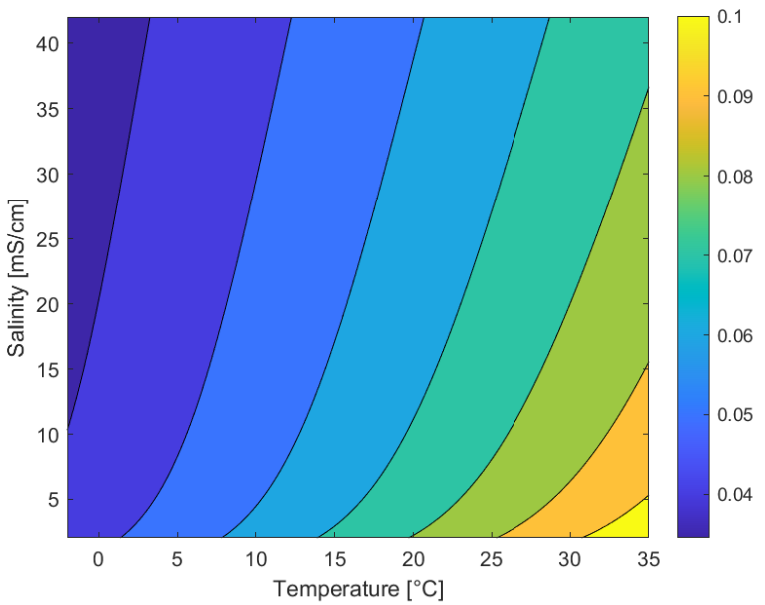

Figure 44: *Numeric deviation of the 'gsw_C_from_SP.m' function to S*

The MATLAB code generating the plot is below:

```
T = -2:0.01:35; % Array of temperature
S = 2:0.05:42;  % Array of salinity

resC=zeros(size(S,2)-1,size(T,2));

for j = 1:size(T,2)
    resC(:,j)=diff(gsw_C_from_SP(S,ones(size(S))*T(j),10.1325));
end

contourf(T,S(1,2:end),resC)
%title('Numerical derivation of the ''gsw\_C\_from\_SP.m'' ...
   function to S')
%subtitle('Stepsize S = 0.05 on PSS-78')
```

```
xlabel('Temperature [\circC]')
ylabel('Salinity [mS/cm]')
colorbar
```

A.5 Equation for TICS Sensor Current

Using MATLAB and the equations given in [17], a not shortend version of the short circuit current Equation (16) is derived. This modulation ignores a potential coupling of the two metal coils as done in [14, 15]. The MATLAB Code uses additional parameters. R_1 and R_4 represent the influence of coil resistance.

```
% Step 1 -  Implementing formulae given in \citep{kang_hui_new_2020}
syms R_1 R_W R_R R_4 L_1 L_2 L_3 L_4 M_12 M_34 N_1 N_4 R_m w real;
syms U1

A = w^2*M_34^2/(R_R+R_4+1i*w*L_4) + R_W+1i*w*L_2+1i*w*L_3;
I_1= A*U1/(A*(R_1+1i*w*L_1)+w^2*M_12^2);
I_2=-1i*w*M_12/A*I_1;
I_4=-1i*w*M_34*I_2/(R_R+R_4+1i*w*L_4);
```

The equation for the sensor current with the terminating resistor $R_R = 0$ is

$$I_4 = -\frac{M_{12}M_{34}\omega^2 \cdot U_1}{\left(\left(R_1 + jL_1\omega\right)\left(R_W + jL_2\omega + jL_3\omega + \frac{M_{34}^2\omega^2}{R_4+jL_4\omega}\right) + M_{12}^2\omega^2\right)\left(R_4 + jL_4\omega\right)} \tag{51}$$

The parameters of this equation are calculated as follow for the purpose of numerical simulation in Section 3.3.2:

The mutual coupling inductance M is calculated with respect to it's indices according to [2, p. 260] to be

$$M_{xy} = k\sqrt{L_x L_y}. \tag{52}$$

A coupling factor of k=1 is used except otherwise is stated. The inductance L_x is calculated with respect to the magnetic resistance of the coil core R_m and the number of turns N ([2, p. 219]) to be

$$L_x = N_x^2 \frac{1}{R_m}. \tag{53}$$

The magnetic resistance of coil is calculated using the core geometry ([2, p. 218]). This is shown in the MATLAB snippet below.

```
%coil cores uncoated
innerD_uc = 14.8*1e-3;%Data sheet TDK ...
    https://www.fair-rite.com/product/toroids-5976011121/
outerD_uc = 25.3*1e-3;%Data sheet TDK
outerR_uc = outerD_uc./2;
innerR_uc = innerD_uc./2;

a_uc = (outerR_uc-innerR_uc);   %height [m]; (B-A)/2 in ...
    https://www.fair-rite.com/product/toroids-5976011121/
b_uc = 11e-3;                   %width [m]; from [16];C in ...
    https://www.fair-rite.com/product/toroids-5976011121/
A_Fe =b_uc*a_uc;
l_Fe =2*pi*(innerR_uc+a_uc/2);    %circumference [m]; U = ...
    2*pi*r; l_Fe average length of core; central core 'fiber'

mu = mu0*muR;
Rm = 1/mu*l_Fe/A_Fe;
```

The coil resistances R_1 and R_4 are calculated based on the coil dimensions. An extra length is added on both sides of the coil model to take the connecting wire sections into account.

```
%cores coated
innerD_c = 13.5*1e-3;%Data sheet TDK
outerD_c = 26.6*1e-3;%Data sheet TDK
outerR_c = outerD_c./2;
innerR_c = innerD_c./2;

a_c = (outerR_c-innerR_c);  %height [m]; (B-A)/2 in ...
    https://www.fair-rite.com/product/toroids-5976011121/
b_c = 11e-3;                %Data sheet TDK

%cables
rho_Cu = 1.68*1e-8; %electrical resistivity [Ohm*m];
l_con = 10e-2; %cable length to connect to circuit [m]. ...
    Arbitrary value.
r_cable = 3e-4; %cable radius [m]. from [16]
l_N1=N1*2*(a_c+b_c+4*r_cable);
l_N4=N4*2*(a_c+b_c+4*r_cable);
l_R1 = 2*l_con+l_N1;
l_R4 = 2*l_con+l_N4;

A_R1=pi*r_cable^2;
```

```
20 A_R4=A_R1;
21 R1 = rho_Cu*l_R1/A_R1;
22 R4 = rho_Cu*l_R4/A_R1;
```

The MATLAB file *'BodeAndSimplificationError.m'* containing the code snippets is on the data media.

A.6 Influence of k on frequency response

Supplemental to content in Section 3.3.2 on the topic of influence of the k-factor.

The comparison of the Bode plots Figure 45a and Figure 45b shows that due to the indeterminacy of the k-factor frequencies in the range of ≤ 100 kHz have to be used. Evaluation in the frequency domain makes the phase shift information insignificant. A closer lock onto Figure 46a and Figure 46b suggests 10 kHz being the best frequency with respect to uncertainty on k-factor and sensor signal strength. An extended examination with different temperature and conductivity values can be found in Figure 47. Note that deviations on phase change with conductivity and tmeperature!

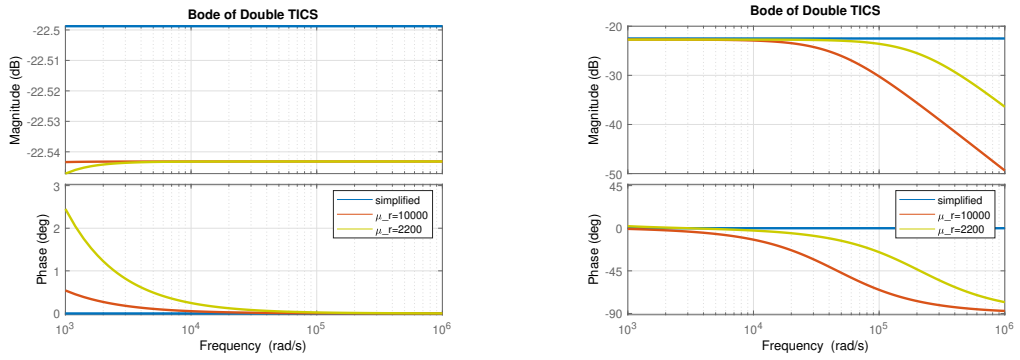

(a) **(b)**

Figure 45: *Bode plots N1=N4=10, μ_r=2200, κ = 75 mS/cm: $k_{12} = k_{34} = 1$ **(a)**; $k_{12} = k_{34} = .99$ **(b)**.*

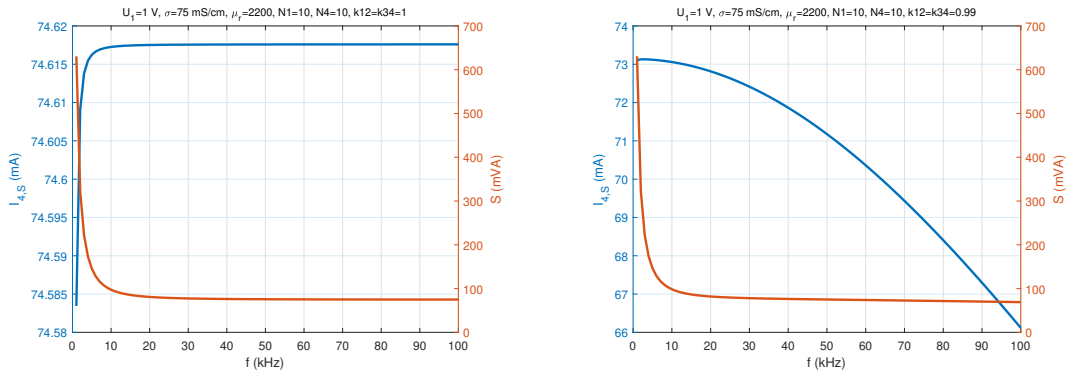

(a) **(b)**

Figure 46: *Frequency dependence of the sensor signal: $k_{12} = k_{34} = 1$ **(a)**; $k_{12} = k_{34} = .99$ **(b)**.*

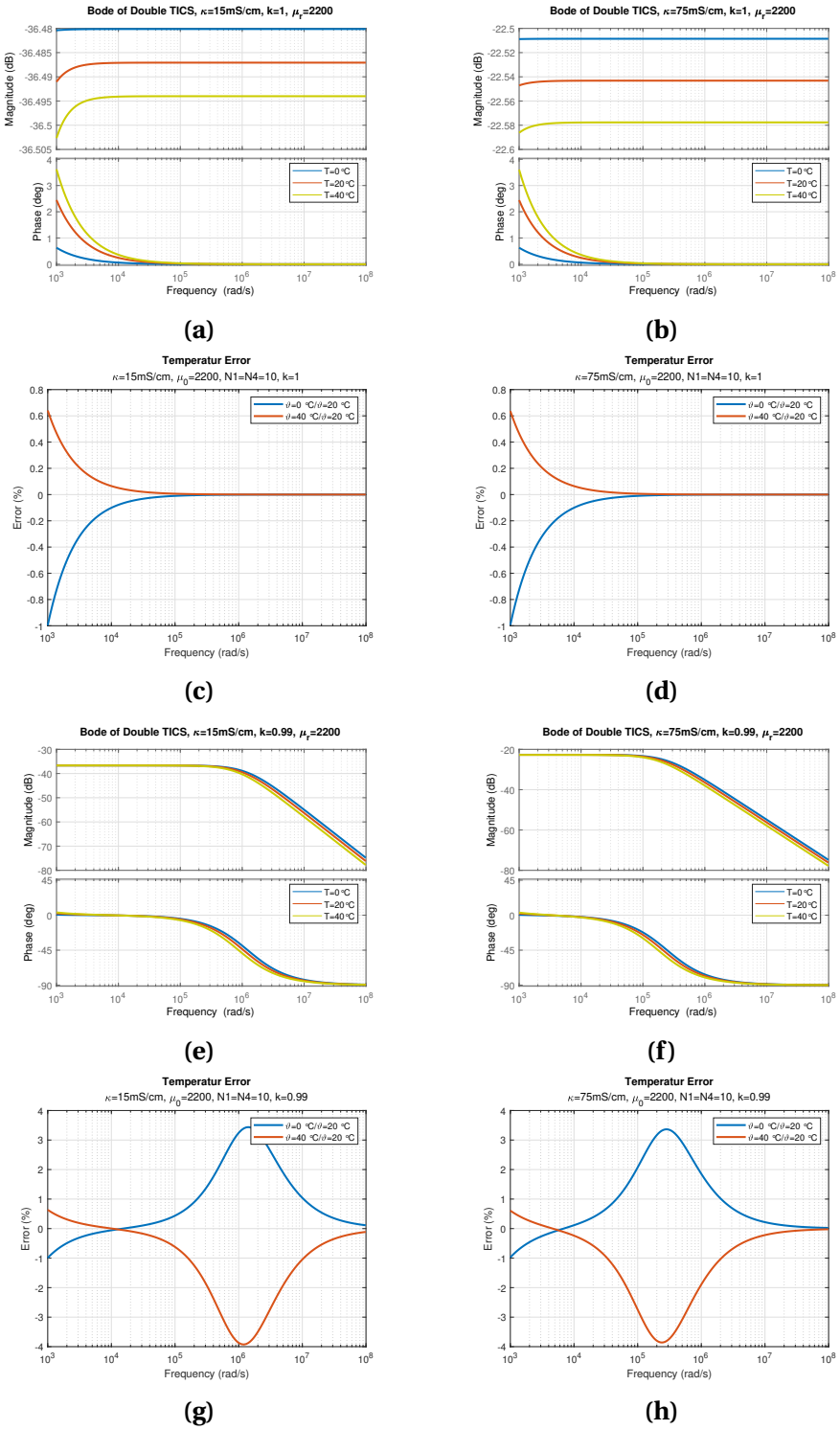

Figure 47: *Temperature influence on Bode and percentage phase deviation for $k_{12} = k_{34} = k$: $\kappa = 15$ms/cm, $k = 1$* ***(a)****; $\kappa = 75$ms/cm, $k = 1$* ***(b)****; $\kappa = 15$ms/cm, $k = 1$* ***(c)****; $\kappa = 75$ms/cm, $k = 1$* ***(d)****; $\kappa = 15$ms/cm, $k = 0.99$* ***(e)****; $\kappa = 75$ms/cm, $k = 0.99$* ***(f)****; $\kappa = 15$ms/cm, $k = 0.99$* ***(g)****; $\kappa = 75$ms/cm, $k = 0.99$* ***(h)****.*

A.7 Effect of Mutual Coupling in Range of MHz

Figure 48 is supplemental to content in Section 3.3.2.

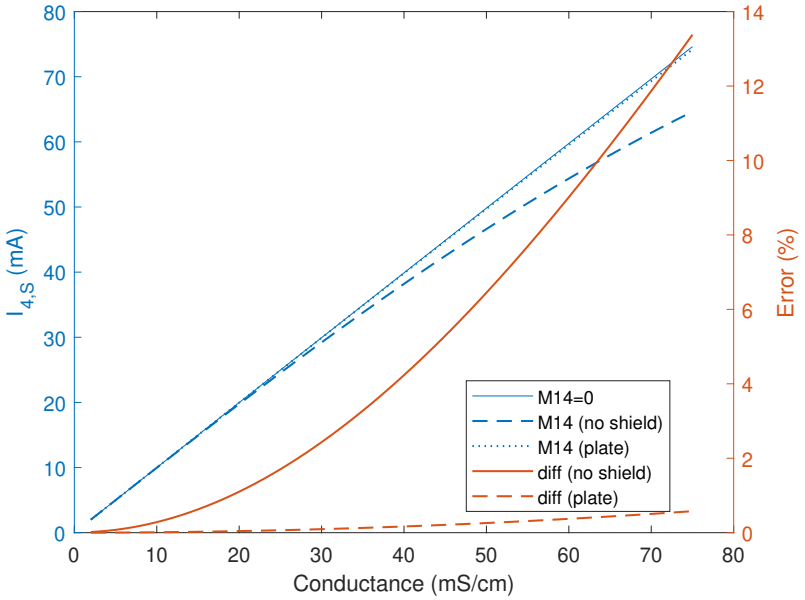

Figure 48: *The influence of M_{14} at 10 MHz*

A.8 Simplifications on k-Factor impact

This section contains simplification and MATLAB code used to derive Equation (28).

The MATLAB code used is

```
% Step 1 -  Implementing formulae given in \citep{kang_hui_new_2020}
syms R_1 R_W R_R R_4 L_1 L_2 L_3 L_4 M_12 M_34 N_1 N_4 R_m w ...
    k_12 k_34 real;
syms U1

A = w^2*M_34^2/(R_R+R_4+1i*w*L_4) + R_W+1i*w*L_2+1i*w*L_3;
I_1= A*U1/(A*(R_1+1i*w*L_1)+w^2*M_12^2);
I_2=-1i*w*M_12/A*I_1;
I_4=-1i*w*M_34*I_2/(R_R+R_4+1i*w*L_4);

% simplifications
I_4sub = simplify(subs(I_4,[R_R, R_1 + L_1*w*1i, R_4 + ...
    L_4*w*1i],[0, L_1*w*1i, L_4*w*1i]))
% rewrite mutual inductance
I_4sub = simplify(subs(I_4sub,[M_12, M_34],[k_12*sqrt(L_1*L_2), ...
    k_34*sqrt(L_3*L_4)]))
% use physical relations
I_4sub = simplify(subs(I_4sub,[L_1, L_2, L_3, ...
    L_4],[N_1^2/R_m,1/R_m,1/R_m, N_4^2/R_m]))
%number of coilt runs always positiv
I_4sub = simplify(subs(I_4sub,[abs(N_1),abs(N_4)],[N_1, N_4])).
```

The assumptions $R_R = 0$, $R_1 << jL_1\omega$, and $R_4 << jL_4\omega$ as well as the Equation (52) and Equation (53) (see Section A.5) are applied.

References

[1] AISLER. *PCB Design Rules | AISLER*. URL: https://aisler.net/help/design-rules-and-specifications/design-rules (visited on 12/06/2021) (cit. on p. 32).

[2] Manfred Albach. *Erfahrungssätze, Bauelemente, Gleichstromschaltungen*. 3., aktualisierte Auflage. Grundlagen der Elektrotechnik. Pearson, 2011. ISBN: 978-3-86894-079-4 (cit. on pp. 2, 5, 58, 59).

[3] Autodesk. *Top 10 Component Placement Tips | EAGLE | Blog*. URL: https://www.autodesk.com/products/eagle/blog/top-10-pcb-component-placement-tips-pcb-beginner/ (visited on 10/14/2021) (cit. on p. 32).

[4] Autodesk. *Top 10 PCB Routing Tips for Beginners | EAGLE | Blog*. URL: https://www.autodesk.com/products/eagle/blog/top-10-pcb-routing-tips-beginners/ (visited on 10/14/2021) (cit. on p. 32).

[5] Herbert Bernstein. *Messelektronik und Sensoren*. Springer Vieweg, 2014. ISBN: 978-3-658-00549-8. DOI: 10.1007/978-3-658-00549-8 (cit. on p. 21).

[6] Niklas Boers. "Observation-based early-warning signals for a collapse of the Atlantic Meridional Overturning Circulation". In: *Nature Climate Change* 11.8 (Aug. 2021). Bandiera_abtest: a Cg_type: Nature Research Journals Number: 8 Primary_atype: Research Publisher: Nature Publishing Group Subject_term: Physical oceanography;Projection and prediction;Statistics Subject_term_id: physical-oceanography;projection-and-prediction;statistics, pp. 680–688. ISSN: 1758-6798. DOI: 10.1038/s41558-021-01097-4. URL: https://www.nature.com/articles/s41558-021-01097-4 (visited on 12/07/2021) (cit. on p. 1).

[7] D. L. Volkov et al. "Meridional overturning circulation and heat transport in the Atlantic Ocean". In: *Bulletin of the American Meteorological Society* 102.8 (Aug. 1, 2021), S176–179. ISSN: 0003-0007, 1520-0477. DOI: 10.1175/2021BAMSStateoftheClimate.1. URL: https://journals.ametsoc.org/view/journals/bams/102/8/2021BAMSStateoftheClimate.1.xml (visited on 10/18/2021) (cit. on p. 1).

[8] A.J. Fougere. "New non-external field inductive conductivity sensor (NXIC) for long term deployments in biologically active regions". In: *OCEANS 2000 MTS/IEEE Conference and Exhibition. Conference Proceedings (Cat. No.00CH37158)*. OCEANS 2000 MTS/IEEE Conference and Exhibition. Conference Proceedings (Cat. No.00CH37158). Vol. 1. Sept. 2000, 623–630 vol.1. DOI: 10.1109/OCEANS.2000.881324 (cit. on p. 14).

[9] Thomas Frey. *Signal- und Systemtheorie*. 2., korrigierte Auflage 2008. Studium. Vieweg Teubner Verlag / GWV Fachverlage GmbH, Wiesbaden, 2009. ISBN: 978-3-8348-9292-8. DOI: 10.1007/978-3-8348-9292-8 (cit. on pp. 22, 23).

[10] *Global Drifter Array*. URL: https://www.aoml.noaa.gov/phod/gdp/interactive/drifter_array.html (visited on 10/14/2021) (cit. on p. 9).

[11] IOC, SCOR, and IAPSO. *The international thermodynamic equation of seawater – 2010: Calculation and use of thermodynamic properties*. Intergovernmental Oceanographic Commission, Manuals and Guides No. 56. UNESCO, 2010. 196 pp. (cit. on pp. 2, 3).

[12] Ralf Jaiser and Jana Kandarr. "Wie beeinflusst der Klimawandel den Jetstream?" In: (2019). Publisher: Earth System Knowledge Platform. DOI: 10.2312/eskp.010. URL: https://www.eskp.de/klimawandel/wie-beeinflusst-der-klimawandel-den-jetstream-9351059/ (visited on 12/07/2021) (cit. on p. 1).

[13] G. C. Johnson et al. "Salinity". In: *Bulletin of the American Meteorological Society* 102.8 (Aug. 1, 2021), S159–164. ISSN: 0003-0007, 1520-0477. DOI: 10.1175/2021BAMSStateoftheClimate.1. URL: https://journals.ametsoc.org/view/journals/bams/102/8/2021BAMSStateoftheClimate.1.xml (visited on 10/18/2021) (cit. on p. 1).

[14] K. Striggow and R. Dankert. "Induktive Leitfähigkeitssensoren für die ozeanologische Anwendung - Physikalische Wirkprinzipien, theoretische Grundlagen und die Möglichkeiten zur Eliminierung des Einflusses einer variablen Kernpermeabilität". In: *Beiträge zur Meereskunde* 50 (1984), pp. 25–41. ISSN: 0067-5148. URL: https://www.io-warnemuende.de/tl_files/forschung/beitraege-zur-meereskunde/1984_50_Beitraege_zur_Meereskunde.pdf (visited on 09/30/2021) (cit. on pp. 5–8, 11, 15, 17, 20, 58).

[15] K. Striggow and R. Dankert. "The exact theory of inductive conductivity sensors for oceanographic application". In: *IEEE Journal of Oceanic Engineering* 10.2 (Apr. 1985), pp. 175–179. ISSN: 0364-9059. DOI: 10.1109/JOE.1985.1145085. URL: http://ieeexplore.ieee.org/document/1145085/ (visited on 09/30/2021) (cit. on pp. 5, 7, 58).

[16] Yiğithan Kandur, Julius Harms, and Thorsten A. Kern. "Uncertainty Analysis for Low-Cost Transformer-Type Inductive Conductivity Sensors". In: *Engineering Proceedings* 6.1 (2021). Number: 1 Publisher: Multidisciplinary Digital Publishing Institute, p. 52. DOI: 10.3390/I3S2021Dresden-10145. URL: https://www.mdpi.com/2673-4591/6/1/52 (visited on 10/15/2021) (cit. on pp. 11, 14, 19, 27, 29, 59).

[17] Song Kang Hui et al. “A new design of inductive conductivity sensor for measuring electrolyte concentration in industrial field”. In: *Sensors and Actuators A: Physical* 301 (Jan. 1, 2020), p. 111761. ISSN: 0924-4247. DOI: 10.1016/j.sna.2019.111761. URL: https://www.sciencedirect.com/science/article/pii/S0924424719315912 (visited on 10/15/2021) (cit. on pp. 11, 14–17, 20, 27, 58).

[18] Walt Kester. *DAC Interface Fundamentals*. URL: https://www.analog.com/media/en/training-seminars/tutorials/MT-019.pdf (visited on 09/22/2021) (cit. on pp. 27, 31).

[19] Ralf Kories and Heinz Schmidt-Walter. *Taschenbuch der Elektrotechnik*. 11., überarbeitete Aufl. Deutsch, 2017. ISBN: 978-3-8085-5865-2 (cit. on pp. 11, 27).

[20] E. Lewis. “The practical salinity scale 1978 and its antecedents”. In: *IEEE Journal of Oceanic Engineering* 5.1 (Jan. 1980). Conference Name: IEEE Journal of Oceanic Engineering, pp. 3–8. ISSN: 1558-1691. DOI: 10.1109/JOE.1980.1145448 (cit. on pp. 2, 3).

[21] Carlos Reyes. “Communication Concept for Multi Sensor Platform”. Master thesis. Hamburg: TUHH, Dec. 2021 (cit. on p. 31).

[22] *Ring-/Doppellochkerne*. TDK Electronics AG. URL: https://www.tdk-electronics.tdk.com/de/186950/produkte/produktkatalog/ferrite-und-zubehoer/epcos-ferrite-und-zubehoer/ringdoubleaperturescores/searchresults?so=%7B%22product_unified_Headline1_en%22%3A%22%22%2C%22product_unified_MATERIAL%22%3A%22N87%22%2C%22product_unified_AL_VALUE%22%3A%22%22%2C%22product_unified_AL_VALUE_TOL%22%3A%22%22%7D (visited on 11/30/2021) (cit. on p. 19).

[23] *SAM D5x/E5x Family Data Sheet*. 2021. URL: https://ww1.microchip.com/downloads/aemDocuments/documents/MCU32/ProductDocuments/DataSheets/SAM_D5x_E5x_Family_Data_Sheet_DS60001507G.pdf (visited on 09/18/2021) (cit. on pp. 26, 27, 31–34, 36).

[24] *Sea Surface Temperature*. Publisher: NASA Earth Observatory. July 31, 2021. URL: https://earthobservatory.nasa.gov/global-maps/MYD28M (visited on 11/25/2021) (cit. on p. 9).

[25] WU Sheng et al. “Investigation of the Performance of an Inductive Seawater Conductivity Sensor”. In: 186.3 (2015), p. 6 (cit. on p. 11).

[26] STMicroelectronics. *Arm Cortex-M4 - Microcontrollers - STMicroelectronics*. Arm® Cortex®-M4 in a nutshell. URL: https://www.st.com/content/st_com/en/arm-32-bit-microcontrollers/arm-cortex-m4.html (visited on 12/06/2021) (cit. on p. 33).

[27] TDK. *Data Sheet Toroid R25.3x14.8x10.0 - TDK*. May 2017. URL: https://www.tdk-electronics.tdk.com/inf/80/db/fer/r_25_3_14_8_10_0.pdf (visited on 08/18/2021) (cit. on p. 27).

[28] *Thermodynamic Equation of SeaWater TEOS-10*. URL: http://teos-10.org/software.htm#1 (visited on 11/25/2021) (cit. on pp. 4, 9, 57).

[29] Ulrich Tietze. *Halbleiter-Schaltungstechnik*. 15., überarbeitete und erweiterte Auflage. Springer Vieweg, 2016. ISBN: 978-3-662-48354-1. DOI: 10.1007/978-3-662-48355-8 (cit. on pp. 13, 14, 20, 21).

[30] Rai Trailokya and Marcoo Zamora. *Voltage Reference Selection and Design Tips For Data Converters*. Application Report. Dallas, Texas, Nov. 2019, p. 12. URL: https://www.ti.com/lit/an/snaa320a/snaa320a.pdf?ts=1632900939983 (cit. on p. 26).

[31] Charles Tsai. *Sine Wave Generation Using PWM With Hercules N2HET and HTU*. Application Report. Texas Instruments, 2015, p. 19. URL: https://www.ti.com/lit/an/spna217/spna217.pdf?ts=1638117052175 (visited on 08/28/2021) (cit. on p. 12).

[32] UNESCO and International Association for the Physical Sciences of the Ocean: Working Group on Symbols, Units {and} Nomenclature in Physical Oceanography. *The International system of units (SI) in oceanography*. Unesco technical papers in marine science 45. Paris: UNESCO, 1985, p. 124. URL: https://unesdoc.unesco.org/ark:/48223/pf0000065031 (visited on 10/20/2021) (cit. on pp. 2, 3).

[33] Deutsche Welle (www.dw.com). *Hochwasser: Diese Rolle spielen Jetstream und Mondumlaufbahn | DW | 16.07.2021*. DW.COM. URL: https://www.dw.com/de/hochwasser-diese-rolle-spielen-jetstream-und-mondumlaufbahn/a-58292603 (visited on 12/07/2021) (cit. on p. 1).

[34] R. T. Wood et al. “A salinity sensor for long-term data collection in estuary studies”. In: *OCEANS 2010 MTS/IEEE SEATTLE*. OCEANS 2010 MTS/IEEE SEATTLE. ISSN: 0197-7385. Sept. 2010, pp. 1–6. DOI: 10.1109/OCEANS.2010.5664602 (cit. on p. 14).

[35] Hank Zumbahlenas and inc Analog Devices, eds. *Linear circuit design handbook*. Amsterdam ; Boston: Elsevier/Newnes Press, 2008. 943 pp. ISBN: 978-0-7506-8703-4 (cit. on p. 32).